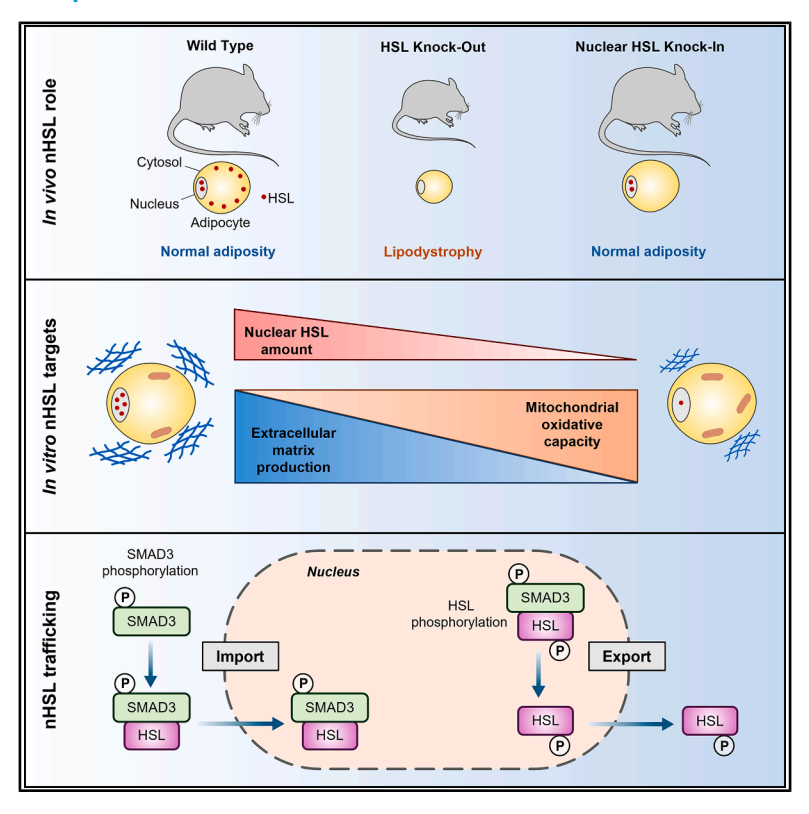
Nuclear hormone-sensitive lipase regulates adipose tissue mass and adipocyte metabolism

Graphical abstract



Authors

Jérémy Dufau, Emeline Recazens, Laura Bottin, ..., Etienne Mouisel, Genevieve Tavernier, Dominique Langin

Correspondence

dominique.langin@inserm.fr

In brief

Dufau, Recazens, et al. identified the neutral lipase HSL in the nucleus of adipocytes, where it modulates gene expression. The trafficking of HSL between the nucleus and the cytosol is under the control of TGF-β and catecholamine signaling. *In vivo*, the presence of nuclear HSL is crucial for adipose tissue development.

Highlights

- Hormone-sensitive lipase is localized within the nuclei of adipocytes
- In vivo, nuclear HSL levels regulate adipose tissue mass
- In vitro, nuclear HSL controls mitochondria and extracellular matrix gene expression
- HSL nuclear level is regulated by TGF-β and PKA signaling pathways









Article

Nuclear hormone-sensitive lipase regulates adipose tissue mass and adipocyte metabolism

Jérémy Dufau,^{1,14} Emeline Recazens,^{1,14} Laura Bottin,¹ Camille Bergoglio,¹ Aline Mairal,¹ Karima Chaoui,² Marie-Adeline Marques,¹ Veronica Jimenez,^{3,4,5} Miquel García,^{3,4,5} Tongtong Wang,⁶ Henrik Laurell,¹ Jason S. Iacovoni,¹ Remy Flores-Flores,¹ Pierre-Damien Denechaud,¹ Khalil Acheikh Ibn Oumar,¹ Ez-Zoubir Amri,⁷ Catherine Postic,⁸ Jean-Paul Concordet,⁹ Pierre Gourdy,^{1,10} Niklas Mejhert,¹¹ Mikael Rydén,¹¹ Odile Burlet-Schiltz,² Fatima Bosch,^{3,4,5} Christian Wolfrum,⁶ Etienne Mouisel,^{1,15} Genevieve Tavernier,^{1,12,15} and Dominique Langin^{1,10,13,16,*}

SUMMARY

In adipocytes, hormone-sensitive lipase (HSL) plays a key role in hydrolyzing triacylglycerols that are stored in lipid droplets. Contrary to the expected phenotype, HSL-deficient mice and humans exhibit lipodystrophy. Here, we show that HSL is also present in the adipocyte nucleus. Mouse models with different HSL subcellular localizations reveal that nuclear HSL is essential for the maintenance of adipose tissue. Gene silencing in human adipocytes shows that HSL, independently of its enzymatic activity, exerts opposing effects on mitochondrial oxidative phosphorylation and the extracellular matrix. Mechanistically, we found that HSL accumulates in the nucleus by interacting with the transforming growth factor β (TGF- β) signaling mediator, mothers against decapentaplegic homolog 3 (SMAD3). Conversely, HSL phosphorylation induces nuclear export. *In vivo*, HSL accumulates in the nucleus of adipocytes during high-fat feeding with the converse effect during fasting. Together, our data show that as both a cytosolic enzyme and a nuclear factor, HSL plays a pivotal role in adipocyte biology and adipose tissue maintenance.

INTRODUCTION

Adipocytes, the parenchymal cells of the adipose tissue, play a key role in regulating energy metabolism by storing fat substrates as triacylglycerols in lipid droplets. ^{1,2} In times of energy deficits, these stores are mobilized by hydrolysis to meet the body's energy demands. During fasting, catecholamines trigger cyclic AMP (cAMP)-dependent protein kinase (PKA)-mediated phosphorylation of hormone-sensitive lipase (HSL), the first rate-limiting enzyme identified as being involved in adipose tissue lipolysis. ^{3,4} HSL phosphorylation on serine residues pro-

motes its translocation from the cytosol to the lipid droplet, where it promotes the hydrolysis of triacylglycerols into free fatty acids and glycerol. 1,5

Biochemical and phylogenetic analyses, however, suggest that HSL performs functions other than the hydrolysis of acylglycerols. HSL is composed of three main structural domains. The N-terminal domain binds the fatty acid binding protein 4 (FABP4), and participates in HSL dimer formation, suggesting that it may be involved in protein-protein interactions. The C-terminal part of the protein contains a catalytic domain and a regulatory domain. The catalytic domain harbors an α/β -hydrolase fold



¹I2MC, Institut des Maladies Métaboliques et Cardiovasculaires, Université de Toulouse, Inserm, Toulouse, France

²IPBS, Institut de Pharmacologie et de Biologie Structurale, Université de Toulouse, CNRS, Toulouse, France

³Center of Animal Biotechnology and Gene Therapy, Universitat Autònoma de Barcelona, Bellaterra, Spain

⁴Department of Biochemistry and Molecular Biology, School of Veterinary Medicine, Universitat Autònoma de Barcelona, Bellaterra, Spain ⁵CIBERDEM, Centro de Investigación Biomédica en Red de Diabetes y Enfermedades Metabólicas Asociadas, Instituto de Salud Carlos III, Madrid, Spain

⁶Institute of Food, Nutrition and Health, ETH Zürich, Schwerzenbach, Switzerland

⁷iBV, Université Côte d'Azur, CNRS, Inserm, Adipo-Cible Research Study Group, Nice, France

⁸Institut Cochin, Université de Paris, CNRS, Inserm, Paris, France

⁹Museum National d'Histoire Naturelle, Inserm, CNRS, Laboratoire Structure et Instabilité des Génomes, Paris, France

¹⁰Centre Hospitalier Universitaire de Toulouse, Toulouse, France

¹¹Department of Medicine (H7), Karolinska Institutet, and Karolinska University Hospital, ME Endokrinologi, Stockholm, Sweden

¹²CREFRE-ANEXPLO, Université de Toulouse, Inserm, Ecole Nationale Vétérinaire de Toulouse, Toulouse, France

¹³IUF, Institut Universitaire de France, Paris, France

¹⁴These authors contributed equally

¹⁵These authors contributed equally

¹⁶Lead contact

^{*}Correspondence: dominique.langin@inserm.fr https://doi.org/10.1016/j.cmet.2025.09.014

Article



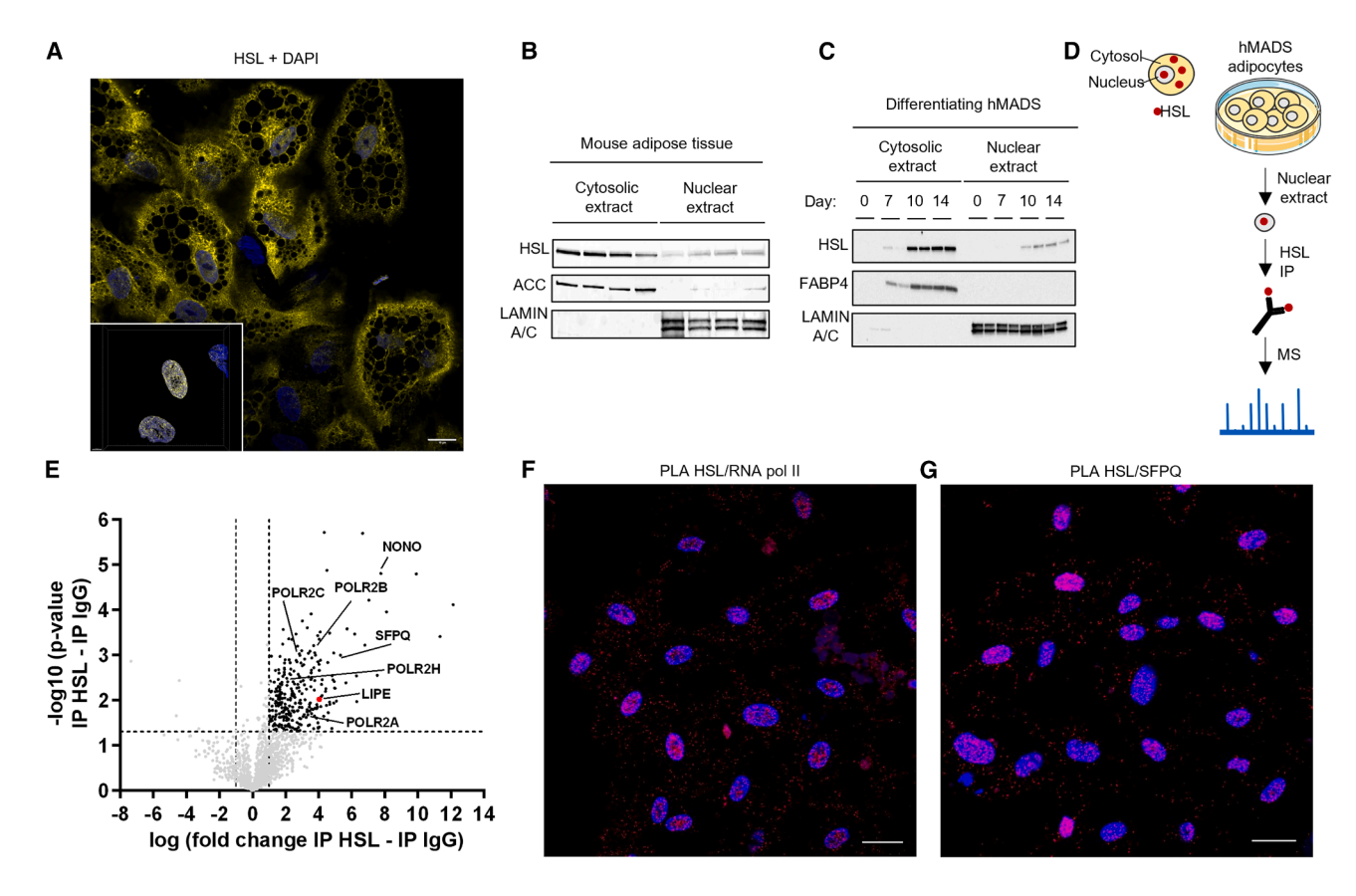


Figure 1. HSL is localized in adipocyte nuclei

(A) HSL immunostaining (yellow) in human multipotent adipose-derived stem cells (hMADS) adipocytes, with 3D reconstitution of a z stack isolating nuclear signal. Nuclei were labeled in blue with Hoechst 33342. Scale bar, 15 μm.

- (B) HSL protein levels in the subcellular fractions of mouse subcutaneous white adipose tissue (n = 4).
- (C) HSL protein levels in the subcellular fractions of differentiating hMADS preadipocytes (n = 2 wells per day from 1 cell passage).
- (D) Experimental design of the characterizations of the nuclear HSL interactome. IP, immunoprecipitation. MS, mass spectrometry.
- (E) Volcano plot of nuclear HSL interactome using immunoprecipitation followed by MS (n = 3 cell passages).
- (F) In situ proximity ligation assays (red signals) using anti-HSL and anti-RNA polymerase II (RNA PolII) antibodies (PLA HSL/RNA Pol II) in hMADS adipocytes. Nuclei were labeled in blue with DAPI. Scale bar, 15 μm.
- (G) In situ proximity ligation assays (red signals) using anti-HSL and anti-SFPQ antibodies (PLA HSL/SFPQ) in hMADS adipocytes. Nuclei were labeled in blue with DAPI. Scale bar, 15 μm.

conserved in prokaryotic and eukaryotic lipases and esterases. The HSL family of enzymes is characterized by a broad substrate specificity. Embedded within the catalytic domain, the intrinsically disordered regulatory domain contains the phosphorylation sites. This region found in mammalian HSL shares no homology with other proteins.

Functions of HSL beyond its lipolytic action are also suggested by the phenotype of HSL-deficient mice. A lack of HSL would be predicted to result in obesity due to deficient acylglycerol hydrolysis, as is the case for mice deficient in another key lipase, adipose triglyceride lipase (ATGL), which, when deficient, results in the expected enlargement of adipose tissue depots. Instead, HSL-deficient mice and humans display a lipodystrophic phenotype, indicating defects in the storage of fats in the adipose tissue. ^{10–12}

To seek an explanation for this discrepant result, we sought to gain a deeper insight into the cellular functions of HSL in adipocytes. In this study, we found that the protein, in addition to its cytoplasmic distribution, is also localized in the adipocyte nu-

cleus. We then explored the role and regulation of nuclear HSL *in vivo* in the control of adipose tissue mass and *in vitro* on human adipocyte metabolism.

RESULTS

HSL is localized in the nuclei of adipocytes

We investigated the subcellular localization of HSL using confocal microscopy, subcellular fractionation, and transmission electron microscopy and found that it was localized in the nucleus of mouse and human adipocytes, where it was associated with chromatin (Figures 1A–1C and S1A–S1D). HSL density was 1.6-fold lower in the nucleus than in the cytosol of human adipocytes (Figure S1E). During adipocyte differentiation, we found a parallel increase in cytoplasmic and nuclear HSL, suggesting that newly synthesized HSL is concomitantly distributed to the two cellular compartments (Figure 1C). We also used nanoliquid chromatography (LC)-tandem mass spectrometry (MS/MS)-based proteomics with intensity-based absolute quantification in the nucleus of th



Cell MetabolismArticle

unbiased approach to assess the level of HSL in adipocyte nuclei (Figures S1F and S1G). To investigate the potential interaction of HSL with nuclear proteins, we performed co-immunoprecipitation of HSL from human adipocyte nuclear extracts (Figure 1D). By proteomic analysis, we identified proteins involved in pre-mRNA processing, including several RNA polymerase II subunits (Figure 1E). We then confirmed the physical interaction of HSL with the C-terminal domain of RNA polymerase II by using a proximity ligation assay (PLA)14 and by co-immunoprecipitation (Figures 1F, S1H, and S1I). A robust interaction was also observed between HSL and the Drosophila behavior/human splicing (DBHS) family proteins, SFPQ (splicing factor proline and glutamine rich) and NONO (non-POU domain-containing octamerbinding protein), which are multifunctional regulators of gene expression (Figures 1G, S1J, and S1K). 15 These data suggest a role of nuclear HSL in the control of gene expression.

In vivo relevance of nuclear HSL

To investigate the *in vivo* significance of nuclear HSL, we developed mouse models through CRISPR-Cas9-mediated gene editing of the *Lipe* locus to alter HSL expression level or subcellular localization (Figure S2A). Bi-allelic deletion of a sequence in exon 6 of *Lipe* resulted in an HSL knockout model (HSL-KO) with neither protein expression nor enzymatic activity of HSL in adipose tissue (Figures S2B–S2D). As previously shown, ^{5,11} we found that the HSL-KO mice were lipodystrophic with decreased fat mass and white fat pad weights (Figures S2E and S2F). Also, the adipose tissue from the HSL-KO mouse was characterized by hypertrophic adipocytes with a heterogeneity of cell size (Figure S2G). ^{10,11} We also observed dysregulation of adipocyte marker expression in HSL-KO mice compared with wild-type (WT) littermates (Figure S2H).

To define a strategy for in vivo investigation of nuclear HSL, we used bioinformatic tools to determine whether the HSL amino acid sequence contains nuclear localization (NLS) or nuclear export (NES) signals. While no in silico analysis predicted an NLS, an NES sequence was predicted in close proximity to the phosphorylation sites (see below). Deletion or modification of this amino acid sequence could alter HSL functions in the cell. Given that the N-terminal domain is involved in protein-protein interactions, 7,8 we decided to add prototypical NLS-coding sequences at the 3' end of the LIPE coding sequence. We found that the addition of an NLS enhanced the nuclear localization of HSL in HEK293T cells and human preadipocytes, neither of which express endogenous HSL (Figures S2I and S2J). Next, we modified the Lipe allele in mouse oocytes to knock in an NLS sequence (Figures 2A and S2A). The resulting mouse model with homozygous HSL-NLS alleles showed nuclear levels of HSL similar to WT mice but markedly blunted cytosolic levels (Figure 2B). Depletion of HSL expression in the cytosolic compartment was associated with almost complete suppression of HSL cytosolic enzymatic activity (Figure S2D). Unlike HSL-KO mice, fat mass, fat pad weights, adipose tissue morphology, and expression of adipocyte markers were not different between HSL-NLS and WT littermates, suggesting that the pool of nuclear HSL is important for the maintenance of adipose tissue (Figures 2C-2F).

To investigate whether nuclear HSL levels serve as a limiting factor in the regulation of adipose tissue mass, we crossed HSL-KO and HSL-NLS homozygous mice (Figure S2K). Unlike HSL-NLS mice, which showed similar HSL levels in adipocyte nuclei compared with control mice, compound heterozygous mice carrying a null allele and an HSL-NLS allele (HSL-KO/HSL-NLS) expressed nuclear HSL at lower levels than littermates carrying a WT allele and an HSL-NLS allele (HSL-WT/HSL-NLS) (Figure S2L). Fat mass percentage and fat pad weights in HSL-KO/HSL-NLS mice were lower than those in HSL-WT/HSL-NLS mice (Figures S2M-S2O). These data suggest that the level of nuclear HSL is limiting for the preservation of adipose tissue mass (Figure S2P).

To show that nuclear HSL is sufficient in a pathophysiological context with expanded adipose tissue, we investigated HSL-KO and HSL-NLS mice after 3 months of high-fat diet feeding. HSL-NLS and WT littermates showed similar fat mass, white fat pad and liver weights, adipose gene expression of adipocyte markers, as well as plasma glucose and insulin levels (Figures 2G–2I and S2Q). Conversely, HSL-KO mice exhibited lipodystrophy, accompanied by hepatomegaly and dysregulation of glucose and insulin levels (Figures 2J–2L and S2R).

HSL is also expressed in the testis⁵ (Figure \$2S). HSL-KO male mice are infertile due to lack of HSL catalytic activity. ^{10,16,17} We found that HSL-NLS male mice were infertile (0 pups from 11 females mated with HSL-NLS homozygous male mice vs. 13 ± 5—mean ± SD—pups from 6 females mated with HSL-WT/HSL-NLS heterozygous male mice). Overall, our results show that the expression of HSL-NLS is sufficient to preserve adipose tissue mass but not male fertility, further supporting a specific role for nuclear HSL in adipocytes (Figure \$2T).

HSL regulates mitochondrial metabolism and extracellular matrix remodeling

HSL interaction with pre-mRNA processing proteins in the adipocyte nucleus suggests a role in the control of gene expression. Therefore, we performed transcriptional profiling of human adipocytes with LIPE small interfering RNA (siRNA)-mediated knockdown, which resulted in both cytosolic and nuclear depletion of HSL (Figures 3A, 3B, and S3A). 18,19 We found that pathways related to transforming growth factor β (TGF- β)-regulated extracellular matrix remodeling were reduced, whereas mitochondrial metabolism pathways were induced in HSL-depleted adipocytes compared with the control cells (Figures 3C and S3B). These results were confirmed by measurements of mRNA levels for mitochondrial oxidative phosphorylation (OXPHOS) and brown/beige adipocyte marker genes, as well as for TGF-β target genes (Figure S3C). Similar data were obtained in adipose stem cell-derived adipocytes from a different donor and in primary human adipocytes derived from stromal vascular progenitor cells (Figures S3D and S3E).20,21 In line with the gene expression data, analysis of the adipocyte secretome revealed lower levels of a large number of TGF-β-regulated peptides in the knockdown cells (Figure 3D). Induction of mitochondrial gene expression was concomitant with increased mitochondrial DNA content, as well as OXPHOS and uncoupling protein 1 (UCP1) protein levels (Figures 3E, 3F, and S3F). Greater mitochondrial protein levels were associated with greater oxygen consumption and fatty acid oxidation in HSL-depleted adipocytes (Figures 3G, 3H, and S3G). Of note, HSL depletion in human beige adipocytes led to similar adaptations, indicating that





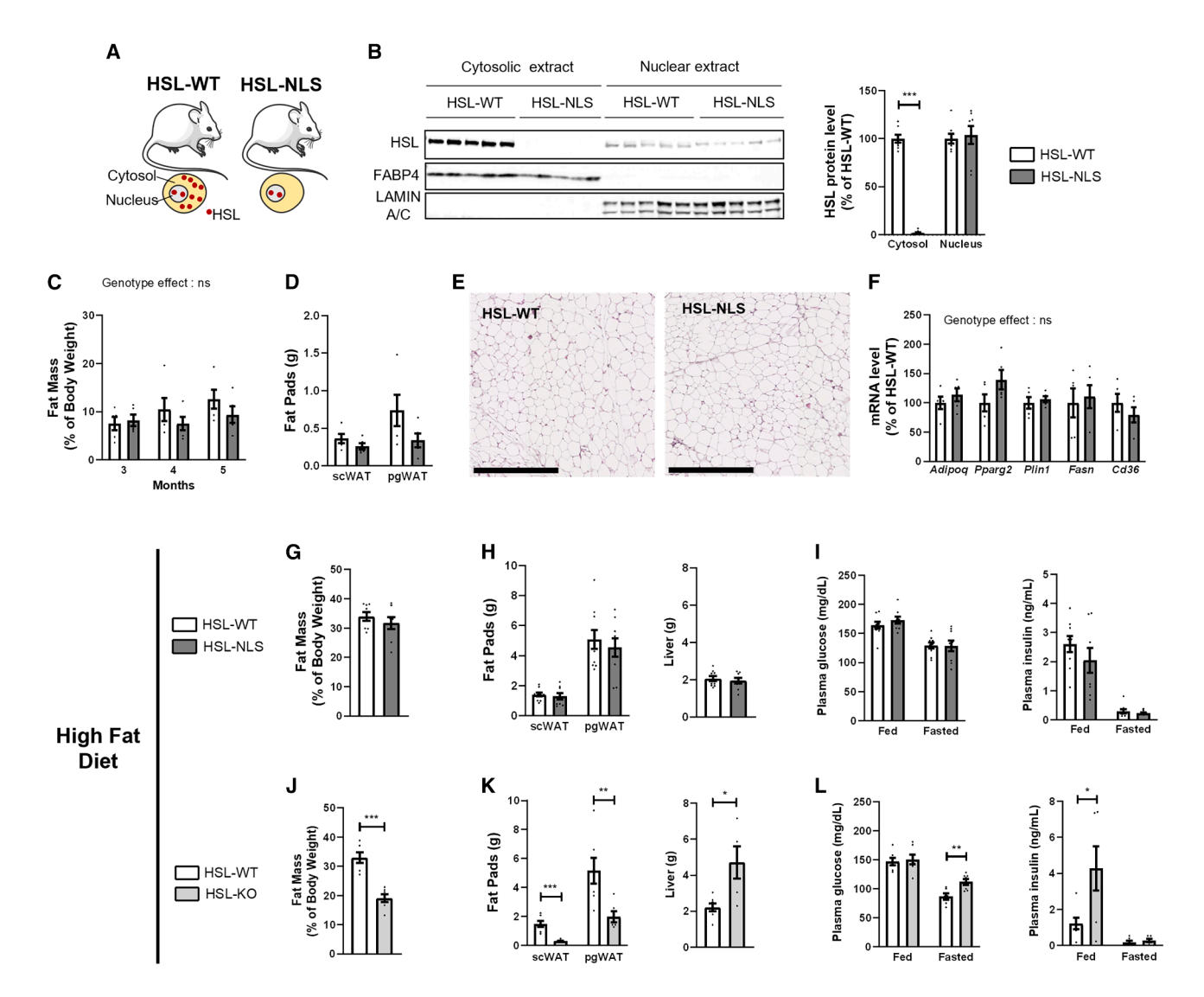


Figure 2. Nuclear HSL regulates adipose tissue mass

(A) Cartoon of HSL-WT and HSL-NLS homozygous mouse models.

(B-F) HSL-WT and HSL-NLS mice were fed a control diet (n=5,5). (B) HSL protein expression in subcellular fractions of white adipose tissue. (C) Whole body fat mass. (D) Subcutaneous (scWAT) and perigonadal (pgWAT) white adipose tissue weights. (E) Bright-field section of adipose tissue. Scale bars, 500 μ m. (F) mRNA levels in white adipose tissue.

(G-I) HSL-WT and HSL-NLS mice were fed a 60% high-fat diet for 12 weeks (n = 10, 9). (G) Whole body fat mass. (H) Weights of scWAT, pgWAT, and liver. (I) Plasma levels of glucose and insulin in fed and fasted mice.

(J-L) HSL-WT and HSL-KO mice were fed a 60% high-fat diet for 12 weeks (n = 7, 6). (J) Whole body fat mass. (K) Weights of scWAT, pgWAT, and liver. (L) Plasma levels of glucose and insulin in fed and fasted mice.

Data are mean ± SEM. *p < 0.05, **p < 0.01, ***p < 0.001 by unpaired Student's t test (B, D, and G-L) and two-way ANOVA with Sidak post hoc test (C and F).

the response to HSL depletion is common to white and beige adipocytes (Figures S3H–S3M), which markedly differ in their mitochondrial activity and secretory capacity. 22,23 These data show that HSL depletion reduces expression of TGF- β -associated targets and increases mitochondrial oxidative phosphorylation.

Nuclear HSL controls mitochondria independently of its enzymatic activity

We assessed the contribution of HSL enzymatic activity to its regulation of mitochondria using different strategies. We transfected HEK293T cells with a vector encoding a naturally occur-

ring catalytically inactive form of HSL (HSL[s]),²⁴ which resulted in lower levels of OXPHOS proteins (Figures S4A and S4B). In human adipocytes, the antilipolytic conditions of cell culture, i.e., the presence of insulin and the lack of agents stimulating cAMP production, kept the lipolytic activity of HSL to a minimum (Figure S4C). Therefore, a reduction in lipolysis is unlikely to contribute to the induction of mitochondrial oxidative phosphorylation observed in HSL-deficient adipocytes (Figure 3). Furthermore, chronic treatment of human adipocytes with an inhibitor that binds to the HSL catalytic site did not modify mitochondrial gene expression in white adipocytes (Figure 4A).²⁵ A lack of an



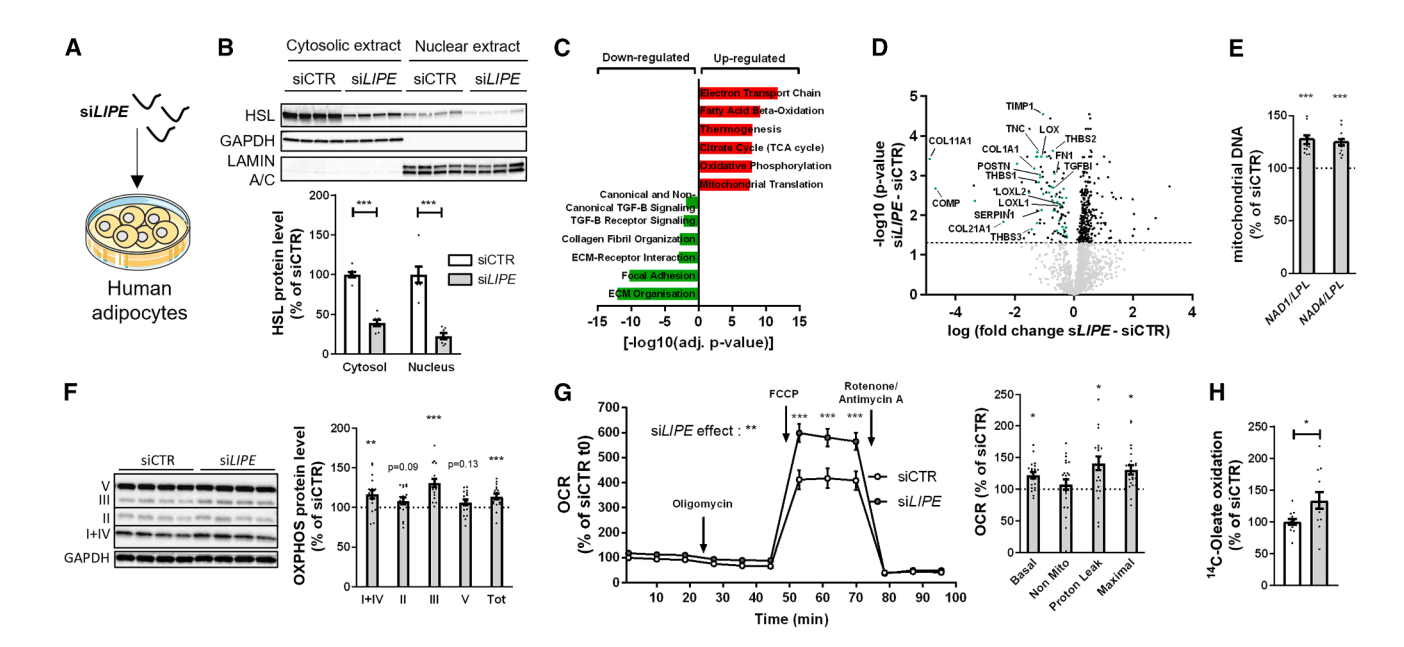


Figure 3. HSL depletion in human adipocytes reduces expression of TGF- β -associated targets and increases mitochondrial oxidative phosphorylation

- (A) Experimental design of LIPE gene silencing in hMADS adipocytes.
- (B) HSL protein level in subcellular fractions (n = 3-4 wells from 2 cell passages).
- (C) Gene ontology and pathway analyses of genes differentially expressed in response to HSL depletion (n = 3).
- (D) Volcano plot of secretome data, green dots show proteins from pathways downregulated in (C) (n = 4 wells from 2 cell passages).
- (E) Ratio of mitochondrial (NAD1 or NAD4) vs. nuclear (LPL) DNA (n = 6 wells from 2 cell passages).
- (F) OXPHOS protein levels (n = 4 wells from 4 cell passages).
- (G) Oxygen consumption rate (OCR) (n = 5-10 wells from 3 cell passages).
- (H) 14 C-Oleate oxidation level (n = 2 wells from 6 cell passages).

Data are mean \pm SEM. *p < 0.05, **p < 0.01, ***p < 0.01, ***p < 0.01 unpaired t test (B, E, and F–H) and two-way ANOVA with Sidak post hoc test (G).

effect on mitochondrial gene expression was also observed following siRNA-mediated depletion of ATGL, encoded by *Pnpla2*, which precedes HSL in the sequential breakdown of triacylglycerol (Figures 4B and S4D). The nuclear receptor peroxisome proliferator-activated receptor γ (PPAR γ) controls mitochondrial biogenesis, and HSL has been suggested to produce endogenous PPAR γ ligands. Thus, we used either a PPAR γ agonist or an antagonist or both together and found that the induction of mitochondrial genes in HSL-depleted adipocytes is independent of PPAR γ activation (Figure 4C). These data show that HSL is a regulator of mitochondrial gene expression in adipocytes independently of its role in lipolysis and PPAR γ activation.

We next wanted to directly study the role of nuclear HSL *in vitro* on mitochondria in cell models that do not express HSL and *in vivo* in mice. Human preadipocytes expressing HSL-NLS showed lower mitochondrial gene expression (Figures S4E and S4F). Expression of HSL-NLS in HEK293T cells resulted in lower OXPHOS mRNA and protein levels associated with diminished basal respiration rate compared with control cells (Figures 4D–4G). *In vivo*, we injected an adeno-associated viral vector expressing a nuclear form of HSL with mutation of the catalytic site serine (HSL-S423A-NLS) into fat pads of HSL haploinsufficient mice (Figure 4H).²⁹ The viral vector injection induced a 1.5-fold higher level of nuclear HSL expression compared with the control-injected mice (Figure 4I). This moder-

ately higher level of nuclear HSL content did not modify body and fat pad weights but did reduce levels of OXPHOS proteins (Figures 4J, 4K, and S4G). As expected for the expression of a catalytically inactive form in the nucleus, there was no change in plasma non-esterified fatty acid or glycerol levels (Figure S4H). However, HSL-S423A-NLS expression was associated with diminished glucose tolerance and greater plasma insulin and glucose levels compared with mice injected with the null vector (Figures 4L and 4M). These data suggest that accumulation of nuclear HSL may impact adipocyte function and systemic metabolism.

HSL mediates the repression of PGC-1 α

The induction of *PPARGC1A* mRNA, encoding PPAR γ coactivator 1- α (PGC-1 α), suggests that the transcriptional co-activator may be involved in mediating the effects of HSL depletion on the mitochondria^{30,31} (Figures S3C, S3E, and S3I). PGC-1 α , but not PGC-1 β , protein levels were higher *in vitro* in adipocytes deficient for HSL compared with control cells (Figures 5A and 5B). HSL-KO mice exhibited higher adipose tissue *PPARGC1A* mRNA and PGC-1 α protein levels compared with HSL-WT mice, a difference not observed in HSL-NLS mice (Figures 5C and 5D). In HSL-depleted white and beige adipocytes, *PPARGC1A* mRNA and pre-mRNA levels were higher compared with controls (Figures 5E and 5F). The degradation rate of *PPARGC1A* mRNA was comparable between control adipocytes

Article



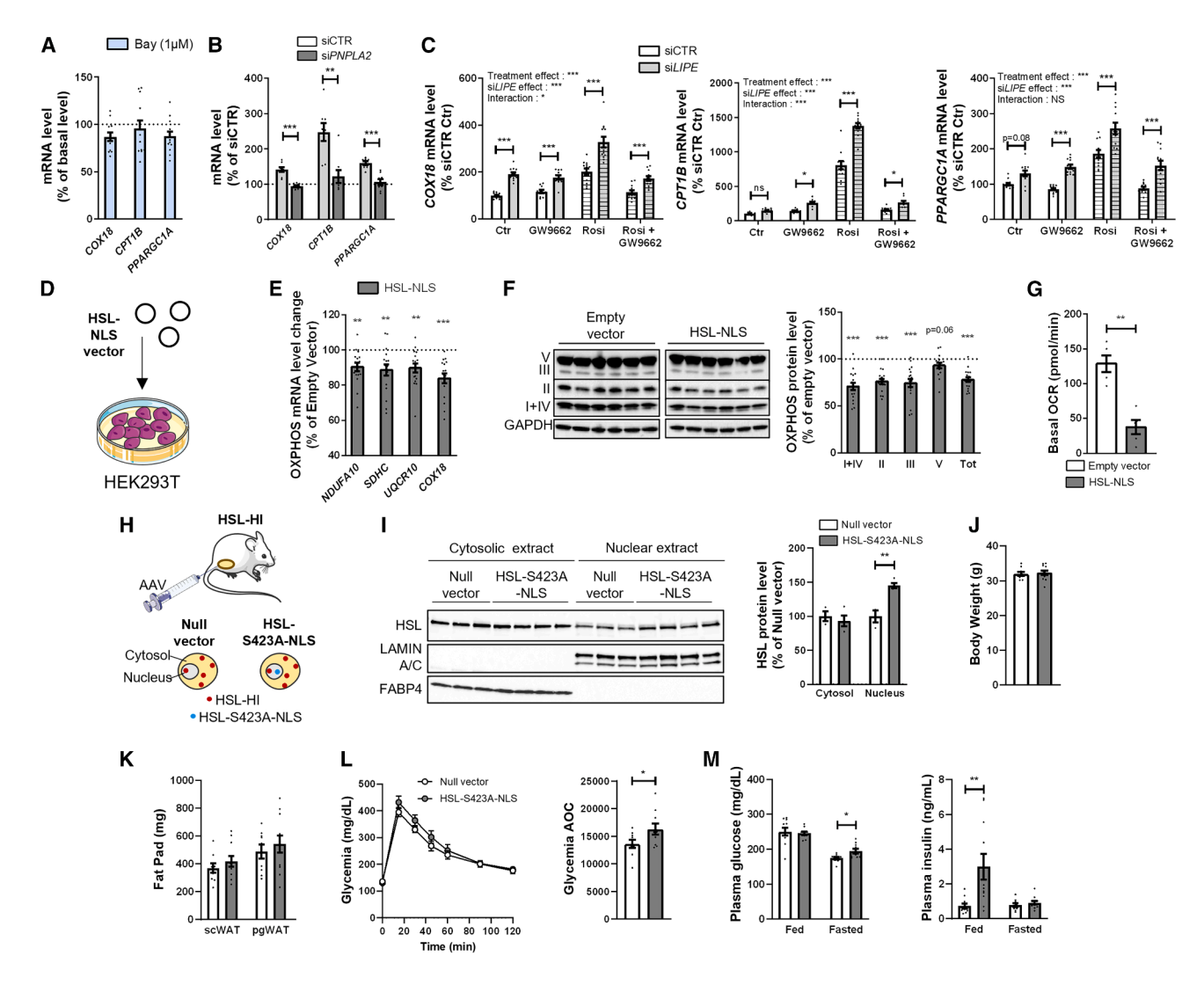


Figure 4. The role of nuclear HSL is independent of its enzymatic activity

(A) mRNA levels in hMADS adipocytes chronically treated with DMSO or the specific HSL inhibitor BAY 59-9435 (n = 6 wells from 2 cell passages).

- (B) mRNA levels in siLIPE-, siPNPLA2-, and siCTR (control siRNA against green fluorescent protein)-treated hMADS adipocytes (n = 4 wells from 2 cell passages).
- (C) mRNA levels in siLIPE- and siCTR-treated hMADS adipocytes treated with the PPARg antagonist GW9662 (10 μ M), the PPARg agonist rosiglitazone (Rosi 0.1 μ M), or both (Rosi + GW9662) (n = 6 replicates from 2 cell passages).
- (D) Experimental design of HEK293T cell transfection using an HSL-NLS-expressing plasmid.
- (E) OXPHOS mRNA levels (n = 6 wells from 3 cell passages).
- (F) OXPHOS protein levels (n = 5-6 wells from 3 cell passages).
- (G) Basal oxygen consumption rate (OCR) (n = 5 wells from 1 cell passage).
- (H) Illustration of mouse injection with adeno-associated viral (AAV) vectors expressing no protein (null) or HSL-S423A-NLS in white adipose tissue of HSL haploinsufficient (HSL-HI) male mice.
- (I) HSL protein levels in subcellular fractions after injection of AAV expressing no protein (null vector, n = 3) or HSL-S423A-NLS (n = 4) in white adipose tissue. (J and K) Body weight (J) and fat pad weights (K) 2 months after AAV injection (n = 9-11).
- (L) Glucose tolerance test in mice 1 month after AAV injection (n = 9, 10).
- (M) Plasma levels of glucose and insulin in fed and fasted mice 1 and 2 months, respectively, after AAV injection (n = 10-11, 9-11).
- Data are mean \pm SEM. *p < 0.05, **p < 0.01, ***p < 0.001 by unpaired Student's t test (A, B, E–G, and I–M) and two-way ANOVA with Sidak post hoc test (C).

and those treated with *LIPE* siRNA, suggesting that HSL acts upstream of *PPARGC1A* pre-mRNA synthesis (Figure 5G). The direct involvement of PGC-1 α in the upregulation of mitochondrial genes was shown in adipocytes transfected with siRNAs targeting *PPARGC1A* (Figure 5H). The induction mediated by HSL depletion (si*LIPE* vs. siCTR, control siRNA against green fluores-

cent protein) was markedly blunted when adipocytes were simultaneously depleted of PGC-1 α (siPPARGC1A/siLIPE vs. siPPARGC1A) (Figure 5I). However, PPARGC1A knockdown had no effect on the downregulation of TGF- β targets induced by HSL depletion (Figure 5J). These data suggest that HSL depletion affects energy metabolism in adipocytes by inducing the



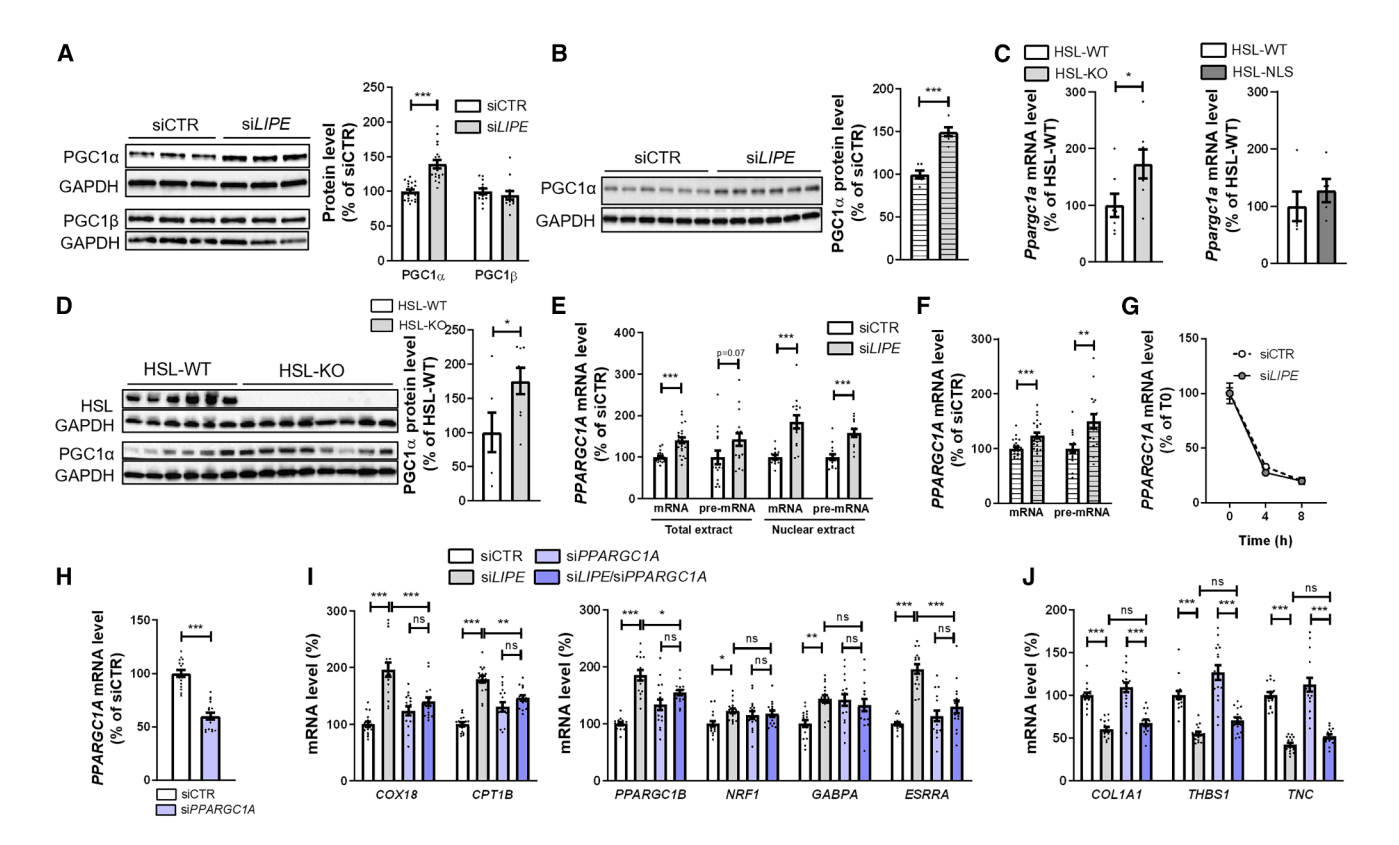


Figure 5. Regulation and role of PGC-1α expression in HSL-depleted adipocytes

- (A) PGC-1 α and PGC-1 β protein levels in hMADS white adipocytes (n = 4–6 from 4 cell passages).
- (B) PGC-1 α protein levels in hMADS beige adipocytes (n = 6 from 1 cell passage).
- (C) PPARGC1A mRNA levels in white adipose tissue of SWISS HSL-KO, HSL-NLS, and their respective HSL-WT littermates (n = 5-7).
- (D) PGC-1 α protein levels in white adipose tissue of male C57BL/6J HSL-KO and HSL-WT mice (n = 6, 8).
- (E) PPARGC1A mRNA and pre-mRNA levels in whole and nuclear extracts of hMADS adipocytes (n = 3-8 wells from 2 to 5 cell passages).
- (F) PPARGC1A mRNA and pre-mRNA levels in whole extracts of siLIPE- and siCTR-treated hMADS beige adipocytes (n = 3-6 wells from 4 to 5 cell passages).
- (G) PPARGC1A mRNA levels in hMADS adipocytes with subsequent actinomycin D treatment (n = 3-4 wells from 3 cell passages).
- (H) PPARGC1A mRNA levels in hMADS adipocytes (n = 4 wells from 4 cell passages).
- (I and J) mRNA levels of hMADS adipocytes treated with various siRNAs (n = 4 wells from 4 cell passages).
- (I) Mitochondrial and cognate transcription factor genes.
- (J) TGF-β target genes.

Data are mean \pm SEM. *p < 0.05, **p < 0.01, ***p < 0.001 by unpaired Student's t test (A–F and H), one-way ANOVA with Tukey post hoc (I and J), and two-way ANOVA with Sidak post hoc test (G).

synthesis of *PPARGC1A* pre-mRNA, whereas the downregulation of TGF- β target genes is driven by alternative mechanisms.

$\text{TGF-}\beta$ signaling regulates the nuclear accumulation of HSL

The downregulation of TGF- β target genes prompted us to investigate the potential modulation of TGF- β signaling in response to HSL depletion. We found that human adipocytes secrete TGF- β 1, whose production is not affected by HSL depletion (Figure S5A). Pharmacological inhibition of TGF- β type I receptor signaling led to a decrease in mRNA levels of *THBS1*, a canonical TGF- β signaling target gene, whereas treatment with recombinant TGF- β 1 resulted in an increase in *THBS1* mRNA levels (Figure S5B). An opposite regulatory effect was observed for *PPARGC1A*. These findings indicate that TGF- β signaling governs the expression of pathways influenced by HSL depletion. To further explore the interdependence between HSL and TGF- β

signaling, we employed combinatorial inhibitory strategies. In HSL-depleted adipocytes, the induction of mitochondrial genes was blunted when type I TGF-β receptor signaling was inhibited (Figure S5C). This suggests that modulation of TGF-β signaling is involved in the response to HSL depletion. Mothers against decapentaplegic homolog (SMAD) 3, a major intracellular effector of TGF-β signaling, could mediate this regulation in human adipocytes, as it has been previously shown to modulate PGC-1a expression in mouse adipose tissue and kidney. 32-34 Similar to TGF-β receptor inhibition, HSL depletion did not induce gene expression of mitochondrial genes when SMAD3 was silenced, suggesting that HSL and SMAD3 work in concert (Figures 6A and S5D). Accordingly, mitochondrial oxygen consumption was not different in adipocytes depleted in SMAD3 alone or in both SMAD3 and HSL (Figure 6B). When type I TGF-β receptor signaling was inhibited and when SMAD3 was silenced, the effect of HSL depletion on the regulation of TGF-β target genes was

Article



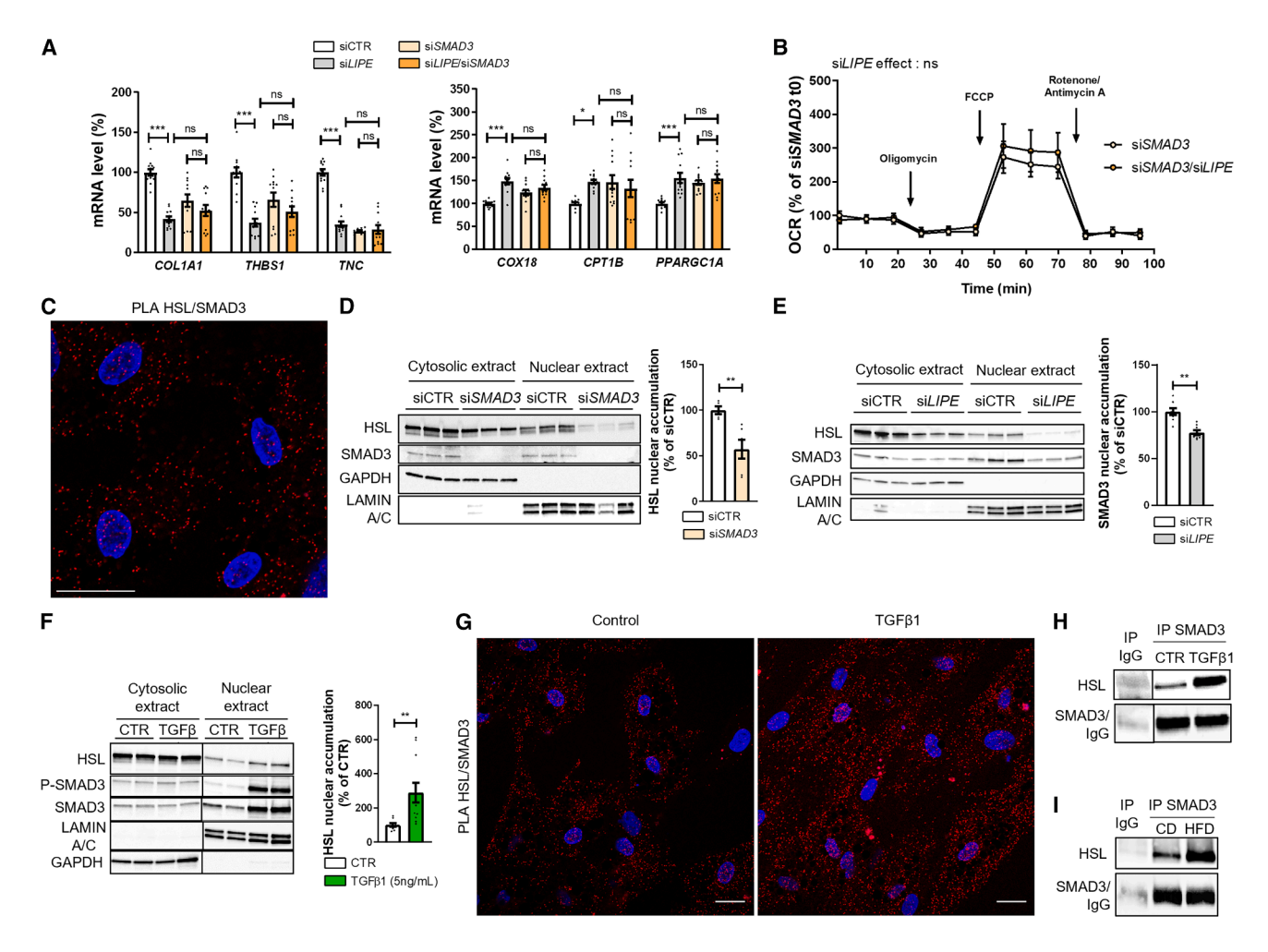


Figure 6. Interaction with SMAD3 controls HSL trafficking into the nucleus

- (A) mRNA levels of hMADS adipocytes treated with various siRNAs (n = 4 wells from 4 cell passages).
- (B) Oxygen consumption rate (OCR) in hMADS adipocytes (n = 3-4 wells from 3 cell passages).
- (C) In situ proximity ligation assays (red signals) using anti-HSL and anti-SMAD3 antibodies (PLA HSL/SMAD3) in hMADS adipocytes. Nuclei were labeled in blue with DAPI. Scale bar, 15 µm.
- (D) HSL protein level in subcellular fractions of hMADS adipocytes treated with siSMAD3 (n = 2-3 wells from 2 cell passages).
- (E) SMAD3 protein levels in subcellular fractions of hMADS adipocytes treated with siLIPE (n = 3-5 wells from 2 cell passages).
- (F) Protein levels of HSL, SMAD3, and phospho-SMAD3 in subcellular fractions of vehicle- (CTR) or TGF-β1-treated hMADS adipocytes (n = 1–3 wells from 4 cell passages).
- (G) In situ proximity ligation assays (red signals) using anti-HSL and anti-SMAD3 antibodies (PLA HSL/SMAD3) in vehicle-treated (control) or TGF-β1-treated hMADS adipocytes. Nuclei were labeled in blue with DAPI. Scale bars, 10 μm.
- (H) Immunoprecipitation of SMAD3 followed by immunodetection of HSL and SMAD3 in whole extracts from vehicle-treated (CTR) and TGF- β 1-treated hMADS adipocytes (n = 2).
- (I) Immunoprecipitation of SMAD3 followed by immunodetection of HSL and SMAD3 in white adipose tissue of mice fed a control (CD) or a 60% high-fat diet (HFD) (n = 2).

Data are mean ± SEM. *p < 0.05, **p < 0.01, ***p < 0.001 by unpaired Student's t test (D-F), one-way ANOVA with Tukey post hoc test (A), and two-way ANOVA (B).

markedly attenuated (Figures 6A and S5C). In the canonical TGF- β pathway, activated SMAD3 binds SMAD4 to form a complex that translocates into the nucleus. ^{35,36} Unlike *SMAD3*, *SMAD4* knockdown did not abrogate the HSL depletion-induced changes in mitochondrial and extracellular matrix gene expression (Figures S5D and S5E). These data suggest that HSL participates in non-canonical TGF- β signaling, regulating the expression of conventional TGF- β targets, such as extracellular matrix genes, and also of mitochondrial genes in adipocytes.

As HSL catalytic activity is not involved in the regulation of gene expression, we tested whether HSL engages in protein-protein interaction with SMAD3. By co-immunoprecipitation and *in situ* proximity ligation assays, we found an interaction between HSL and SMAD3 in the cytosolic and nuclear compartments of adipocytes (Figures 6C, S6A, and S6B) and in HEK293T cells expressing nuclear HSL (Figure S6C). We did not observe an interaction between HSL and SMAD4 (Figures S6D and S6E). Depletion of SMAD3 but not of SMAD4 reduced levels of nuclear HSL in



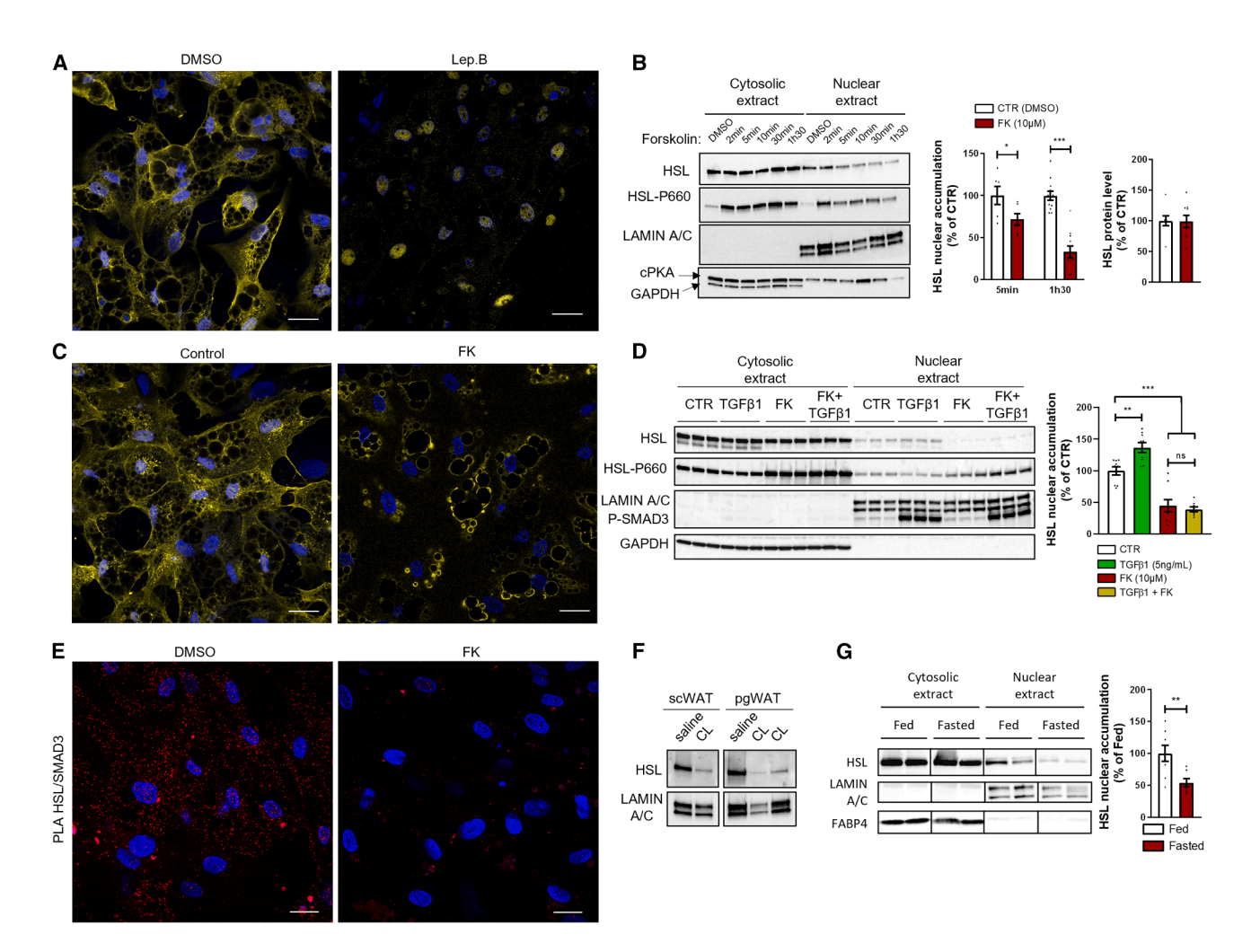


Figure 7. PKA signaling controls the export of nuclear HSL

(A) HSL immunostaining (yellow) in DMSO-treated or leptomycin B (Lep.B)-treated hMADS adipocytes. Nuclei were labeled in blue with DAPI. Scale bars, 15 μ m. (B) Protein levels of HSL, phospho-HSL (HSL-P660), and the catalytic subunit of PKA (cPKA) in subcellular fractions (n = 1-4 wells from 9 cell passages) and in total cell extract (n = 2-4 wells from 3 cell passages) of DMSO-treated and forskolin (FK)-treated hMADS adipocytes.

- (C) HSL immunostaining (yellow) in DMSO- (control) and FK-treated hMADS adipocytes. Nuclei were labeled in blue with DAPI. Scale bars, 15 µm.
- (D) Protein levels of HSL, phospho-HSL (HSL-P660), and phospho-SMAD3 in subcellular fractions of DMSO-treated (CTR), FK-, TGF- β 1-, or FK- and TGF- β 1-treated (FK + TGF- β 1) hMADS adipocytes (n = 3 wells from 3 cell passages).
- (E) In situ proximity ligation assays (red signals) using anti-HSL and anti-SMAD3 antibodies in DMSO-treated or FK-treated hMADS adipocytes. Nuclei were labeled in blue with DAPI. Scale bars, 10 µm.
- (F) Immunodetection of HSL in sorted adipocyte nuclei from subcutaneous (scWAT) and perigonadal (pgWAT) white adipose tissue of mice treated with saline or the β_3 -adrenergic receptor agonist CL-316,243 (n = 1-2).
- (G) HSL protein levels in subcellular fractions of white adipose tissue from mice in fed or fasted state (n = 8-7).

Data are mean ± SEM. **p < 0.01, ***p < 0.001 by unpaired Student's t test (B and G) and one-way ANOVA with Tukey post hoc (D).

adipocytes (Figures 6D and S6F). Conversely, depletion of HSL diminished SMAD3 nuclear content (Figure 6E). Treatment of human adipocytes with recombinant TGF-β1 induced phosphorylation and nuclear translocation of SMAD3, as well as nuclear accumulation of HSL, without altering the phosphorylation status of HSL (Figures 6F and S6G). Furthermore, TGF-β1 treatment enhanced the formation of SMAD3/HSL and SMAD3/SMAD4 complexes but did not promote an interaction between SMAD4 and HSL in human adipocyte nuclei (Figures 6G, 6H, and S6H). Recombinant TGF-β1 also increased HSL nuclear accumulation ex vivo in mouse adipose tissue explants (Figure S6I). These data reveal that TGF-β-mediated activation of SMAD3 induces

the formation of canonical SMAD3/SMAD4 and cell-specific SMAD3/HSL complexes. In mice with diet-induced obesity, we observed an increase in the formation of HSL/SMAD3 complexes and HSL accumulation in adipocyte nuclei (Figures 6I and S6J). The SMAD3/HSL complex favors the nuclear import of HSL and could therefore contribute to the increase of HSL nuclear content in a pathophysiological context.

PKA signaling regulates nuclear HSL export

Following investigation of the mechanism of import, we studied the export of HSL from the nucleus to the cytosol. Treatment of human adipocytes with leptomycin B, an inhibitor of the exportin 1

Article



(chromosomal region maintenance 1, CRM1), led to nuclear accumulation of HSL (Figures 7A and S7A), indicating that HSL, like SMAD4,³⁷ must be continuously shuttling between the nucleus and the cytoplasm. In line with these data, the prediction algorithms, LocNES and NetNES, identified a potential NES located in the regulatory domain of HSL (Figure S7B).^{5,38,39} Deletion of the predicted sequence resulted in accumulation of the mutant HSL protein in the nuclei of HEK293T cells (Figure S7C).

During lipolysis, HSL is phosphorylated by PKA on specific sites in the regulatory domain.⁵ These sites are located close to the NES (Figure S7B). Treatment of human adipocytes with the adenylyl cyclase activator, forskolin, promoted a decrease in nuclear HSL content and favored its localization to the lipid droplet surface without alterations in total HSL protein content (Figures 7B and 7C). 40 Consistent with nuclear HSL phosphorylation, the catalytic subunit of PKA is present in human adipocyte nuclei (Figure 7B). Combined treatment with TGF-β1 and forskolin revealed that the latter was predominant over the former in regulating HSL nuclear localization (Figure 7D). HSL nuclear export induced by forskolin was accompanied by a diminution of HSL interaction with SMAD3 in adipocyte nuclei without alterations of SMAD3 nuclear content (Figures 7E, S7D, and S7E). Similar to forskolin treatment, glucose and insulin deprivation of human adipocytes, which triggers a fasting-like condition in vitro, induced HSL phosphorylation and nuclear export (Figures S7F-S7H). Such cAMP-dependent regulation was also shown in vivo in mouse adipocytes. Isolated adipocyte nuclei from mice acutely treated with a β_3 -adrenergic receptor agonist, CL316,243, showed decreased nuclear HSL content in fat depots (Figure 7F).41 Furthermore, we found that the HSL nuclear content was lower in the fasted state compared with the fed state (Figure 7G). Together, these data argue that HSL relocation from the nucleus to the lipid droplet is regulated by PKA and its nuclear content is modulated by fasting.

DISCUSSION

Since its initial identification, 4 HSL has been regarded as a cytosolic enzyme involved in adipocyte lipolysis. However, the HSL protein family serves diverse functions in all three domains of life.⁵ In plants, an HSL-like protein devoid of enzymatic activity, the gibberellin receptor GID1, is localized in the nucleus.⁴² In bacteria, another member of the HSL family, Aes, inhibits MalT, a transcriptional activator of maltose metabolism genes, through protein-protein interaction. 43,44 Here, we show that HSL is localized within the adipocyte nucleus. Mice with cytosolic depletion of HSL but preserved nuclear expression did not develop lipodystrophy, a phenotype observed both in mice and humans with complete HSL deficiency. 10-12 Moreover, nuclear HSL levels appear to be a limiting factor in the regulation of adipose tissue mass. Furthermore, overexpression of nuclear HSL resulted in adverse effects on glucose homeostasis, suggesting that a precise nuclear HSL concentration is critical for proper adipocyte function. The nuclear localization of HSL in adipocytes thus implies a significant role in adipose tissue biology that is independent of its cytosolic functions.

In adipocytes, HSL is a component of a complex that includes the TGF- β signaling mediator SMAD3. The interaction between HSL and SMAD3 favors the translocation of both proteins into

the nucleus and the expression of conventional TGF- β target genes. These genes encode components of the extracellular matrix, ⁴⁵ whose secretion is regulated by HSL. Interactions between SMAD3 and HSL as well as between SMAD3 and SMAD4 appear to be mutually exclusive. ³⁵ HSL is therefore a novel cell type-specific regulatory factor of the TGF- β pathway. The nature of the extracellular matrix genes regulated by the SMAD3/HSL and SMAD3/SMAD4 complexes is not yet known.

In human fibroblasts, TGF- β signaling provides a cell-autonomous connection between the extracellular matrix and mitochondria. This pathway is evolutionarily conserved. We show that, in adipocyte nuclei, HSL is involved in the repression of *PPARGC1A* pre-mRNA synthesis, which in turn downregulates mitochondrial metabolism. The negative regulation of mitochondrial metabolism remains poorly documented. We identify a dynamic inhibitory pathway operational in white and beige adipocytes, revealing that HSL action is independent of and additional to the canonical beigeing transcriptional program.

Upon catecholamine stimulation of adipocytes, the dynamic inhibition of mitochondrial metabolism by TGF- β is abrogated. Mechanistically, this is mediated by PKA, which, upon activation by catecholamines, phosphorylates HSL in its regulatory domain, conferring the propensity of HSL for interorganellar trafficking. This phosphorylation event leads to nuclear export of HSL, which eliminates transcriptional repression of *PPARGC1A*. Lifting this inhibitory pathway may facilitate the catecholamine-induced transcriptional activation by ATF/CREB. ⁴⁷ This work raises the question of the interdependence between ATF/CREB activation and HSL nuclear export in the induction of mitochondrial metabolism.

During the development of obesity, adipose tissue production of TGF- β and extracellular matrix increases, 33,48 whereas sensitivity to catecholamine-induced lipolysis is impaired. 49 In mice, diet-induced obesity and insulin resistance result in an opposite regulation of TGF- β and mitochondrial gene expression in adipocytes. 50 An increase in adipocyte nuclear HSL content may contribute to adipocyte dysfunction, such as extracellular matrix deposition and impaired mitochondrial metabolism, and associated dysregulation of systemic metabolism. $^{45,51-53}$

We provide evidence that nuclear HSL contributes to the maintenance of adipose tissue mass. Furthermore, the transport of adipocyte HSL between the nucleus, the cytosol, and lipid droplets allows for a coordinated control of three major pathways of triacylglycerol metabolism, lipolysis, *de novo* lipogenesis, and fatty acid oxidation. 4,19 In terms of signaling pathways, HSL appears to be a node connecting the PKA and TGF- β pathways. Fine-tuning of nuclear HSL levels may be essential to ensure proper adipocyte function.

Limitations of the study

In vitro experiments were performed under conditions of reduced HSL enzymatic activity. HSL engages with a broad spectrum of nuclear proteins in adipocytes; however, the functional implications of these interactions remain unclear. Notably, the involvement of HSL in the transcriptional repression of *PPARGC1A* requires further elucidation. Our findings indicate that HSL interacts with SFPQ and NONO, both members of the DBHS protein family. ¹⁵ DBHS proteins are implicated in multiple stages of gene expression, including transcription, RNA splicing



Cell Metabolism Article

and editing, RNA transport, and translation.⁵⁴ Additionally, they form dynamic dimers with various partners, suggesting adipocyte-specific functions for HSL in these processes that remain to be elucidated. Of particular relevance, PSPC1, another DBHS family member, has been shown to promote adipogenesis in vitro and contribute to adipose tissue mass expansion in vivo. 55 Our findings provide evidence that nuclear export of HSL follows a well-characterized pathway involving PKA-mediated phosphorylation and classical exportin-dependent transport. Mutating the phosphorylation sites within the HSL regulatory domain could provide information on NES-mediated nuclear export. The mechanisms governing SMAD3-mediated nuclear import remain unclear. The specific protein domains mediating HSL-SMAD3 interaction have yet to be identified. Furthermore, SMAD3 participates in signaling pathways beyond TGF-β type I receptor signaling in adipocytes. HSL may contribute to SMAD3-mediated transcriptional regulation in pathways other than canonical TGF-β signaling. In vivo, the molecular basis of lipodystrophy in HSL-deficient mice and humans remains unclear. Male sterility precludes direct comparison between HSL-KO and HSL-NLS mice obtained by crossing double heterozygous mice. Each genotype was therefore compared with its respective WT counterparts. The mechanisms implicating HSL in adipose tissue maintenance remain unclear and may involve both enzymatic and non-enzymatic activities of HSL. Expression of HSL with an intact or mutated catalytic site, whose expression is restricted to the nucleus or cytosol, may provide insights.

RESOURCE AVAILABILITY

Lead contact

Dominique Langin (dominique.langin@inserm.fr) is the lead contact for this manuscript and should be contacted for further information and requests for resources and reagents.

Materials availability

Unique reagents generated in this study are available from the lead contact with a completed materials transfer agreement.

Data and code availability

- Uncropped scans and source data are available as Data S1.
- No proprietary data or code is associated with this manuscript.
- Any additional information required to reanalyze the data reported in this
 paper is available from the lead contact upon request.

ACKNOWLEDGMENTS

We thank Bruno Antonny (IPMC, CNRS Université Côte d'Azur), Gautier Langin (ZMBP, Universität Tübingen), Cedric Moro (I2MC, Toulouse), Matthew Harms (AstraZeneca, Gothenburg), Lenka Rossmeislova, and Michaela Siklova (Third Faculty of Medicine, Charles University, Prague) for critical reading of the manuscript. Alice Brion contributed to the design of the CRISPR-Cas9 gene editing strategy (Museum National d'Histoire Naturelle, Paris, France). Marie Lou Calmy, Julie Tanios, Marie Rebeaud, Alexandra Montagner, Anaïs Bodon, and Stéphanie Cassant-Sourdy (I2MC, Toulouse) provided experimental help. Xavier León Madrenas contributed to adeno-associated viral vector production (Center of Animal Biotechnology and Gene Therapy, Universitat Autònoma de Barcelona). The following technological facilities contributed to the work: GenoToul Anexplo (Morgane Rousseau, Guillaume Morera, CREFRE, Toulouse), GenoToul GeT-TRiX (Yannick Lippi, ToxAlim, Toulouse), GenoToul GeT Health (Emeline Lhuillier, I2MC, Toulouse), GenoToulTRI (Christèle Ségura, I2MC; Bruno Payré, CMEAB, Toulouse), and WeMet (Alexandre Lucas, I2MC, Toulouse). This work was supported by Inserm, Université de Toulouse, the European Foundation for the Study of Diabetes (EFSD/Novo Nordisk Programme for Diabetes Research in Europe 2019 to D.L.), Fondation pour la Recherche Médicale (DEQ20170336720 to D.L.), Agence Nationale de la Recherche (ANR-17-CE14-0015 Hepadialogue to C.P. and D.L.; ANR-23-IAHU-0011 IHU Health Age to D.L.), Région Occitanie (to D.L.), AstraZeneca France (to D.L.), and the European Research Council (ERC) under the European Union's Horizon 2020 research and innovation program (SPHERES, ERC Synergy Grant agreement no. 856404 to M.R. and D.L.). Proteomic work was supported in part by Région Occitanie, Fonds Européens de Développement Régional (FEDER) and the REACT-EU program, Toulouse Métropole, and by the French Ministry of Research (PIA, "Infrastructures Nationales en Biologie et Santé" program, Proteomics French Infrastructure [ProFI, UAR2048] project, and ANR-10-INBS-08 to O.B.-S.). F.B. received support from MCIN/AEI/10.13039/501100011033 (PID2020-113864RB-100), Spain.

AUTHOR CONTRIBUTIONS

Conceptualization, J.D., E.R., and D.L.; methodology, J.D., E.R., R.F.-F., G.T., and D.L.; investigation, J.D., E.R., L.B., C.B., A.M., M.-A.M., T.W., H.L., R.F.-F., K.A.I.O., E.M., and G.T.; 'omic data analyses, J.D., K.C., J.S.I., and O.B.-S.; design and production of AAV, V.J., M.G., and F.B.; writing—original draft, J.D., E.R., and D.L.; writing—review & editing, J.D., E.R., H.L., J.S.I., P.-D.D., E.-Z.A., C.P., J.-P.C., P.G., N.M., M.R., F.B., C.W., E.M., G.T., and D.L.; funding acquisition, D.L., E.-Z.A., C.P., M.R., and O.B.-S.; resources, G.T. and K.A.I.O.; supervision, D.L.

DECLARATION OF INTERESTS

The authors declare no competing interests.

STAR*METHODS

Detailed methods are provided in the online version of this paper and include the following:

- KEY RESOURCES TABLE
- EXPERIMENTAL MODEL AND STUDY PARTICIPANT DETAILS
 - Mouse models
 - Cell models
- METHOD DETAILS
 - o Measurements in human cells
 - o Measurements in mouse models
 - o Measurements common to mouse and human models
- QUANTIFICATION AND STATISTICAL ANALYSIS

SUPPLEMENTAL INFORMATION

Supplemental information can be found online at https://doi.org/10.1016/j.cmet.2025.09.014.

Received: March 18, 2025 Revised: August 18, 2025 Accepted: September 28, 2025 Published: October 23, 2025

REFERENCES

- Morigny, P., Boucher, J., Arner, P., and Langin, D. (2021). Lipid and glucose metabolism in white adipocytes: pathways, dysfunction and therapeutics. Nat. Rev. Endocrinol. 17, 276–295. https://doi.org/10.1038/ s41574-021-00471-8.
- Sakers, A., De Siqueira, M.K., Seale, P., and Villanueva, C.J. (2022).
 Adipose-tissue plasticity in health and disease. Cell 185, 419–446. https://doi.org/10.1016/j.cell.2021.12.016.
- Guilherme, A., Rowland, L.A., Wang, H., and Czech, M.P. (2023). The adipocyte supersystem of insulin and cAMP signaling. Trends Cell Biol. 33, 340–354. https://doi.org/10.1016/j.tcb.2022.07.009.

Article



- Vaughan, M., Berger, J.E., and Steinberg, D. (1964). Hormone-Sensitive Lipase and Monoglyceride Lipase Activities in Adipose Tissue. J. Biol. Chem. 239, 401–409. https://doi.org/10.1016/S0021-9258(18)51692-6.
- Recazens, E., Mouisel, E., and Langin, D. (2021). Hormone-sensitive lipase: sixty years later. Prog. Lipid Res. 82, 101084. https://doi.org/10. 1016/j.plipres.2020.101084.
- Osterlund, T. (2001). Structure-function relationships of hormone-sensitive lipase. Eur. J. Biochem. 268, 1899–1907. https://doi.org/10.1046/j. 1432-1327.2001.02097.x.
- Krintel, C., Klint, C., Lindvall, H., Mörgelin, M., and Holm, C. (2010). Quarternary structure and enzymological properties of the different hormone-sensitive lipase (HSL) isoforms. PLoS One 5, e11193. https://doi.org/10.1371/journal.pone.0011193.
- Smith, A.J., Thompson, B.R., Sanders, M.A., and Bernlohr, D.A. (2007). Interaction of the adipocyte fatty acid-binding protein with the hormone-sensitive lipase: regulation by fatty acids and phosphorylation. J. Biol. Chem. 282, 32424–32432. https://doi.org/10.1074/jbc.M703730200.
- Haemmerle, G., Lass, A., Zimmermann, R., Gorkiewicz, G., Meyer, C., Rozman, J., Heldmaier, G., Maier, R., Theussl, C., Eder, S., et al. (2006). Defective lipolysis and altered energy metabolism in mice lacking adipose triglyceride lipase. Science 312, 734–737. https://doi.org/10.1126/science.1123965.
- Osuga, J., Ishibashi, S., Oka, T., Yagyu, H., Tozawa, R., Fujimoto, A., Shionoiri, F., Yahagi, N., Kraemer, F.B., Tsutsumi, O., et al. (2000). Targeted disruption of hormone-sensitive lipase results in male sterility and adipocyte hypertrophy, but not in obesity. Proc. Natl. Acad. Sci. USA 97, 787–792. https://doi.org/10.1073/pnas.97.2.787.
- Wang, S.P., Laurin, N., Himms-Hagen, J., Rudnicki, M.A., Levy, E., Robert, M.F., Pan, L., Oligny, L., and Mitchell, G.A. (2001). The adipose tissue phenotype of hormone-sensitive lipase deficiency in mice. Obes. Res. 9, 119–128. https://doi.org/10.1038/oby.2001.15.
- Albert, J.S., Yerges-Armstrong, L.M., Horenstein, R.B., Pollin, T.I., Sreenivasan, U.T., Chai, S., Blaner, W.S., Snitker, S., O'Connell, J.R., Gong, D.W., et al. (2014). Null mutation in hormone-sensitive lipase gene and risk of type 2 diabetes. N. Engl. J. Med. 370, 2307–2315. https:// doi.org/10.1056/NEJMoa1315496.
- Schwanhäusser, B., Busse, D., Li, N., Dittmar, G., Schuchhardt, J., Wolf, J., Chen, W., and Selbach, M. (2011). Global quantification of mammalian gene expression control. Nature 473, 337–342. https://doi.org/10.1038/ nature10098.
- Söderberg, O., Gullberg, M., Jarvius, M., Ridderstråle, K., Leuchowius, K. J., Jarvius, J., Wester, K., Hydbring, P., Bahram, F., Larsson, L.G., et al. (2006). Direct observation of individual endogenous protein complexes in situ by proximity ligation. Nat. Methods 3, 995–1000. https://doi.org/10.1038/nmeth947
- Knott, G.J., Bond, C.S., and Fox, A.H. (2016). The DBHS proteins SFPQ, NONO and PSPC1: a multipurpose molecular scaffold. Nucleic Acids Res. 44, 3989–4004. https://doi.org/10.1093/nar/gkw271.
- Vallet-Erdtmann, V., Tavernier, G., Contreras, J.A., Mairal, A., Rieu, C., Touzalin, A.M., Holm, C., Jégou, B., and Langin, D. (2004). The testicular form of hormone-sensitive lipase HSLtes confers rescue of male infertility in HSL-deficient mice. J. Biol. Chem. 279, 42875–42880. https://doi.org/ 10.1074/jbc.M403495200.
- Wang, S.P., Wu, J.W., Bourdages, H., Lefebvre, J.F., Casavant, S., Leavitt, B.R., Labuda, D., Trasler, J., Smith, C.E., Hermo, L., et al. (2014). The catalytic function of hormone-sensitive lipase is essential for fertility in male mice. Endocrinology 155, 3047–3053. https://doi.org/10.1210/en.2014-1031.
- Bezaire, V., Mairal, A., Ribet, C., Lefort, C., Girousse, A., Jocken, J., Laurencikiene, J., Anesia, R., Rodriguez, A.M., Ryden, M., et al. (2009). Contribution of adipose triglyceride lipase and hormone-sensitive lipase to lipolysis in hMADS adipocytes. J. Biol. Chem. 284, 18282–18291. https://doi.org/10.1074/jbc.M109.008631.
- Morigny, P., Houssier, M., Mairal, A., Ghilain, C., Mouisel, E., Benhamed, F., Masri, B., Recazens, E., Denechaud, P.D., Tavernier, G., et al. (2019). Interaction between hormone-sensitive lipase and ChREBP in fat cells

- controls insulin sensitivity. Nat. Metab. 1, 133–146. https://doi.org/10.1038/s42255-018-0007-6.
- Rodriguez, A.M., Pisani, D., Dechesne, C.A., Turc-Carel, C., Kurzenne, J. Y., Wdziekonski, B., Villageois, A., Bagnis, C., Breittmayer, J.P., Groux, H., et al. (2005). Transplantation of a multipotent cell population from human adipose tissue induces dystrophin expression in the immunocompetent mdx mouse. J. Exp. Med. 201, 1397–1405. https://doi.org/10.1084/jem. 20042224.
- Mazzucotelli, A., Viguerie, N., Tiraby, C., Annicotte, J.S., Mairal, A., Klimcakova, E., Lepin, E., Delmar, P., Dejean, S., Tavernier, G., et al. (2007). The transcriptional coactivator peroxisome proliferator activated receptor (PPAR)gamma coactivator-1 alpha and the nuclear receptor PPAR alpha control the expression of glycerol kinase and metabolism genes independently of PPAR gamma activation in human white adipocytes. Diabetes 56, 2467–2475. https://doi.org/10.2337/db06-1465.
- Barquissau, V., Beuzelin, D., Pisani, D.F., Beranger, G.E., Mairal, A., Montagner, A., Roussel, B., Tavernier, G., Marques, M.A., Moro, C., et al. (2016). White-to-brite conversion in human adipocytes promotes metabolic reprogramming towards fatty acid anabolic and catabolic pathways. Mol. Metab. 5, 352–365. https://doi.org/10.1016/j.molmet.2016. 03.002.
- Scheja, L., and Heeren, J. (2019). The endocrine function of adipose tissues in health and cardiometabolic disease. Nat. Rev. Endocrinol. 15, 507–524. https://doi.org/10.1038/s41574-019-0230-6.
- Laurell, H., Grober, J., Vindis, C., Lacombe, T., Dauzats, M., Holm, C., and Langin, D. (1997). Species-specific alternative splicing generates a catalytically inactive form of human hormone-sensitive lipase. Biochem. J. 328, 137–143. https://doi.org/10.1042/bj3280137.
- Langin, D., Dicker, A., Tavernier, G., Hoffstedt, J., Mairal, A., Rydén, M., Arner, E., Sicard, A., Jenkins, C.M., Viguerie, N., et al. (2005). Adipocyte lipases and defect of lipolysis in human obesity. Diabetes 54, 3190– 3197. https://doi.org/10.2337/diabetes.54.11.3190.
- Puigserver, P., and Spiegelman, B.M. (2003). Peroxisome proliferatoractivated receptor-gamma coactivator 1 alpha (PGC-1 alpha): transcriptional coactivator and metabolic regulator. Endocr. Rev. 24, 78–90. https://doi.org/10.1210/er.2002-0012.
- Schupp, M., and Lazar, M.A. (2010). Endogenous ligands for nuclear receptors: digging deeper. J. Biol. Chem. 285, 40409–40415. https://doi.org/10.1074/jbc.R110.182451.
- Shen, W.J., Yu, Z., Patel, S., Jue, D., Liu, L.F., and Kraemer, F.B. (2011). Hormone-sensitive lipase modulates adipose metabolism through PPARγ. Biochim. Biophys. Acta 1811, 9–16. https://doi.org/10.1016/j. bbalip.2010.10.001.
- Girousse, A., Tavernier, G., Valle, C., Moro, C., Mejhert, N., Dinel, A.L., Houssier, M., Roussel, B., Besse-Patin, A., Combes, M., et al. (2013). Partial inhibition of adipose tissue lipolysis improves glucose metabolism and insulin sensitivity without alteration of fat mass. PLoS Biol. 11, e1001485. https://doi.org/10.1371/journal.pbio.1001485.
- Puigserver, P., Wu, Z., Park, C.W., Graves, R., Wright, M., and Spiegelman, B.M. (1998). A cold-inducible coactivator of nuclear receptors linked to adaptive thermogenesis. Cell 92, 829–839. https://doi.org/ 10.1016/s0092-8674(00)81410-5.
- Tiraby, C., Tavernier, G., Lefort, C., Larrouy, D., Bouillaud, F., Ricquier, D., and Langin, D. (2003). Acquirement of brown fat cell features by human white adipocytes. J. Biol. Chem. 278, 33370–33376. https://doi.org/10. 1074/jbc.M305235200.
- Kang, H.M., Ahn, S.H., Choi, P., Ko, Y.A., Han, S.H., Chinga, F., Park, A.S. D., Tao, J., Sharma, K., Pullman, J., et al. (2015). Defective fatty acid oxidation in renal tubular epithelial cells has a key role in kidney fibrosis development. Nat. Med. 21, 37–46. https://doi.org/10.1038/nm.3762.
- Yadav, H., Quijano, C., Kamaraju, A.K., Gavrilova, O., Malek, R., Chen, W., Zerfas, P., Zhigang, D., Wright, E.C., Stuelten, C., et al. (2011). Protection from obesity and diabetes by blockade of TGF-β/Smad3 signaling. Cell Metab. 14, 67–79. https://doi.org/10.1016/j.cmet.2011.04.013.



Cell Metabolism Article

- Bahn, Y.J., Wang, Y., Dagur, P., Scott, N., Cero, C., Long, K.T., Nguyen, N., Cypess, A.M., and Rane, S.G. (2024). TGF-beta antagonism synergizes with PPARgamma agonism to reduce fibrosis and enhance beige adipogenesis. Mol. Metab. 90, 102054. https://doi.org/10.1016/j.molmet. 2024.102054.
- David, C.J., and Massagué, J. (2018). Contextual determinants of TGFbeta action in development, immunity and cancer. Nat. Rev. Mol. Cell Biol. 19, 419–435. https://doi.org/10.1038/s41580-018-0007-0.
- Derynck, R., and Budi, E.H. (2019). Specificity, versatility, and control of TGF-beta family signaling. Sci. Signal. 12, eaav5183. https://doi.org/10. 1126/scisignal.aav5183.
- Pierreux, C.E., Nicolás, F.J., and Hill, C.S. (2000). Transforming growth factor beta-independent shuttling of Smad4 between the cytoplasm and nucleus. Mol. Cell. Biol. 20, 9041–9054. https://doi.org/10.1128/MCB. 20.23.9041-9054.2000.
- Ia Cour, T., Kiemer, L., Mølgaard, A., Gupta, R., Skriver, K., and Brunak, S. (2004). Analysis and prediction of leucine-rich nuclear export signals. Protein Eng. Des. Sel. 17, 527–536. https://doi.org/10.1093/protein/qzh062.
- Xu, D., Marquis, K., Pei, J., Fu, S.C., Cağatay, T., Grishin, N.V., and Chook, Y.M. (2015). LocNES: a computational tool for locating classical NESs in CRM1 cargo proteins. Bioinformatics 31, 1357–1365. https://doi.org/10. 1093/bioinformatics/btu826.
- Egan, J.J., Greenberg, A.S., Chang, M.K., Wek, S.A., Moos, M.C., Jr., and Londos, C. (1992). Mechanism of hormone-stimulated lipolysis in adipocytes: translocation of hormone-sensitive lipase to the lipid storage droplet. Proc. Natl. Acad. Sci. USA 89, 8537–8541. https://doi.org/10. 1073/pnas.89.18.8537.
- Sun, W., Dong, H., Balaz, M., Slyper, M., Drokhlyansky, E., Colleluori, G., Giordano, A., Kovanicova, Z., Stefanicka, P., Balazova, L., et al. (2020). snRNA-seq reveals a subpopulation of adipocytes that regulates thermogenesis. Nature 587, 98–102. https://doi.org/10.1038/s41586-020-2856-x.
- Ueguchi-Tanaka, M., Ashikari, M., Nakajima, M., Itoh, H., Katoh, E., Kobayashi, M., Chow, T.Y., Hsing, Y.I., Kitano, H., Yamaguchi, I., et al. (2005). GIBBERELLIN INSENSITIVE DWARF1 encodes a soluble receptor for gibberellin. Nature 437, 693–698. https://doi.org/10.1038/nature04028.
- Joly, N., Danot, O., Schlegel, A., Boos, W., and Richet, E. (2002). The Aes protein directly controls the activity of MaIT, the central transcriptional activator of the Escherichia coli maltose regulon. J. Biol. Chem. 277, 16606–16613. https://doi.org/10.1074/jbc.M200991200.
- Schiefner, A., Gerber, K., Brosig, A., and Boos, W. (2014). Structural and mutational analyses of Aes, an inhibitor of MalT in Escherichia coli. Proteins 82, 268–277. https://doi.org/10.1002/prot.24383.
- Henegar, C., Tordjman, J., Achard, V., Lacasa, D., Cremer, I., Guerre-Millo, M., Poitou, C., Basdevant, A., Stich, V., Viguerie, N., et al. (2008).
 Adipose tissue transcriptomic signature highlights the pathological relevance of extracellular matrix in human obesity. Genome Biol. 9, R14. https://doi.org/10.1186/gb-2008-9-1-r14.
- Zhang, H., Tsui, C.K., Garcia, G., Joe, L.K., Wu, H., Maruichi, A., Fan, W., Pandovski, S., Yoon, P.H., Webster, B.M., et al. (2024). The extracellular matrix integrates mitochondrial homeostasis. Cell 187, 4289–4304.e26. https://doi.org/10.1016/j.cell.2024.05.057.
- Herzig, S., Long, F., Jhala, U.S., Hedrick, S., Quinn, R., Bauer, A., Rudolph, D., Schutz, G., Yoon, C., Puigserver, P., et al. (2001). CREB regulates hepatic gluconeogenesis through the coactivator PGC-1. Nature 413, 179–183. https://doi.org/10.1038/35093131.
- Alessi, M.C., Bastelica, D., Morange, P., Berthet, B., Leduc, I., Verdier, M., Geel, O., and Juhan-Vague, I. (2000). Plasminogen activator inhibitor 1, transforming growth factor-beta1, and BMI are closely associated in human adipose tissue during morbid obesity. Diabetes 49, 1374–1380. https://doi.org/10.2337/diabetes.49.8.1374.
- Arner, P., and Langin, D. (2014). Lipolysis in lipid turnover, cancer cachexia, and obesity-induced insulin resistance. Trends Endocrinol. Metab. 25, 255–262. https://doi.org/10.1016/j.tem.2014.03.002.

- Roh, H.C., Kumari, M., Taleb, S., Tenen, D., Jacobs, C., Lyubetskaya, A., Tsai, L.T.Y., and Rosen, E.D. (2020). Adipocytes fail to maintain cellular identity during obesity due to reduced PPARgamma activity and elevated TGFbeta-SMAD signaling. Mol. Metab. 42, 101086. https://doi.org/10. 1016/j.molmet.2020.101086.
- 51. Klimcáková, E., Roussel, B., Márquez-Quiñones, A., Kovácová, Z., Kováciková, M., Combes, M., Siklová-Vítková, M., Hejnová, J., Srámková, P., Bouloumié, A., et al. (2011). Worsening of obesity and metabolic status yields similar molecular adaptations in human subcutaneous and visceral adipose tissue: decreased metabolism and increased immune response. J. Clin. Endocrinol. Metab. 96, E73–E82. https://doi.org/10.1210/jc.2010-1575.
- Schöttl, T., Kappler, L., Fromme, T., and Klingenspor, M. (2015). Limited OXPHOS capacity in white adipocytes is a hallmark of obesity in laboratory mice irrespective of the glucose tolerance status. Mol. Metab. 4, 631–642. https://doi.org/10.1016/j.molmet.2015.07.001.
- 53. Vila, I.K., Badin, P.M., Marques, M.A., Monbrun, L., Lefort, C., Mir, L., Louche, K., Bourlier, V., Roussel, B., Gui, P., et al. (2014). Immune cell Toll-like receptor 4 mediates the development of obesity- and endotoxemia-associated adipose tissue fibrosis. Cell Rep. 7, 1116–1129. https://doi.org/10.1016/j.celrep.2014.03.062.
- Takeiwa, T., Ikeda, K., Horie, K., and Inoue, S. (2024). Role of RNA binding proteins of the Drosophila behavior and human splicing (DBHS) family in health and cancer. RNA Biol. 21, 459–475. https://doi.org/10.1080/ 15476286.2024.2332855.
- Wang, J., Rajbhandari, P., Damianov, A., Han, A., Sallam, T., Waki, H., Villanueva, C.J., Lee, S.D., Nielsen, R., Mandrup, S., et al. (2017). RNAbinding protein PSPC1 promotes the differentiation-dependent nuclear export of adipocyte RNAs. J. Clin. Invest. 127, 987–1004. https://doi. org/10.1172/JCl89484.
- Haemmerle, G., Zimmermann, R., Hayn, M., Theussl, C., Waeg, G., Wagner, E., Sattler, W., Magin, T.M., Wagner, E.F., and Zechner, R. (2002). Hormone-sensitive lipase deficiency in mice causes diglyceride accumulation in adipose tissue, muscle, and testis. J. Biol. Chem. 277, 4806–4815. https://doi.org/10.1074/jbc.M110355200.
- 57. Recazens, E., Tavernier, G., Dufau, J., Bergoglio, C., Benhamed, F., Cassant-Sourdy, S., Marques, M.A., Caspar-Bauguil, S., Brion, A., Monbrun, L., et al. (2022). ChREBPbeta is dispensable for the control of glucose homeostasis and energy balance. JCl Insight 7, e153431. https://doi.org/10.1172/jci.insight.153431.
- Concordet, J.P., and Haeussler, M. (2018). CRISPOR: intuitive guide selection for CRISPR/Cas9 genome editing experiments and screens.
 Nucleic Acids Res. 46, W242–W245. https://doi.org/10.1093/nar/gky354.
- Vion, J., Sramkova, V., Montastier, E., Marquès, M.A., Caspar-Bauguil, S., Duparc, T., Martinez, L.O., Bourlier, V., Harant, I., Larrouy, D., et al. (2021).
 Metabolic and cardiovascular adaptations to an 8-wk lifestyle weight loss intervention in younger and older obese men. Am. J. Physiol. Endocrinol. Metab. 321, E325–E337. https://doi.org/10.1152/ajpendo.00109.2021.
- Skurk, T., Ecklebe, S., and Hauner, H. (2007). A novel technique to propagate primary human preadipocytes without loss of differentiation capacity. Obesity (Silver Spring) 15, 2925–2931. https://doi.org/10.1038/oby.2007.349
- Dufau, J., Shen, J.X., Couchet, M., De Castro Barbosa, T., Mejhert, N., Massier, L., Griseti, E., Mouisel, E., Amri, E.Z., Lauschke, V.M., et al. (2021). In vitro and ex vivo models of adipocytes. Am. J. Physiol. Cell Physiol. 320, C822–C841. https://doi.org/10.1152/ajpcell.00519.2020.
- Rossmeislová, L., Malisová, L., Kracmerová, J., Tencerová, M., Kovácová, Z., Koc, M., Siklová-Vítková, M., Viquerie, N., Langin, D., and Stich, V. (2013). Weight loss improves the adipogenic capacity of human preadipocytes and modulates their secretory profile. Diabetes 62, 1990–1995. https://doi.org/10.2337/db12-0986.
- 63. Ribet, C., Montastier, E., Valle, C., Bezaire, V., Mazzucotelli, A., Mairal, A., Viguerie, N., and Langin, D. (2010). Peroxisome proliferator-activated receptor-alpha control of lipid and glucose metabolism in human white

Article



- adipocytes. Endocrinology 151, 123–133. https://doi.org/10.1210/en. 2009-0726.
- Legland, D., Arganda-Carreras, I., and Andrey, P. (2016). MorphoLibJ: integrated library and plugins for mathematical morphology with ImageJ. Bioinformatics 32, 3532–3534. https://doi.org/10.1093/bioinformatics/btw413.
- Schindelin, J., Arganda-Carreras, I., Frise, E., Kaynig, V., Longair, M., Pietzsch, T., Preibisch, S., Rueden, C., Saalfeld, S., Schmid, B., et al. (2012). Fiji: an open-source platform for biological-image analysis. Nat. Methods 9, 676–682. https://doi.org/10.1038/nmeth.2019.
- Mori, D., Grégoire, C., Voisinne, G., Celis-Gutierrez, J., Aussel, R., Girard, L., Camus, M., Marcellin, M., Argenty, J., Burlet-Schiltz, O., et al. (2021). The T cell CD6 receptor operates a multitask signalosome with opposite functions in T cell activation. J. Exp. Med. 218, e20201011. https://doi. org/10.1084/jem.20201011.
- 67. Jimenez, V., Muñoz, S., Casana, E., Mallol, C., Elias, I., Jambrina, C., Ribera, A., Ferre, T., Franckhauser, S., and Bosch, F. (2013). In vivo adeno-associated viral vector-mediated genetic engineering of white and

- brown adipose tissue in adult mice. Diabetes 62, 4012–4022. https://doi.org/10.2337/db13-0311.
- Holm, C., Olivecrona, G., and Ottosson, M. (2001). Assays of lipolytic enzymes. Methods Mol. Biol. 155, 97–119. https://doi.org/10.1385/1-59259-231-7:097.
- Virtue, S., and Vidal-Puig, A. (2021). GTTs and ITTs in mice: simple tests, complex answers. Nat. Metab. 3, 883–886. https://doi.org/10.1038/ s42255-021-00414-7.
- Kuleshov, M.V., Jones, M.R., Rouillard, A.D., Fernandez, N.F., Duan, Q., Wang, Z., Koplev, S., Jenkins, S.L., Jagodnik, K.M., Lachmann, A., et al. (2016). Enrichr: a comprehensive gene set enrichment analysis web server 2016 update. Nucleic Acids Res. 44, W90–W97. https://doi.org/10.1093/ nar/gkw377.
- Xie, Z., Bailey, A., Kuleshov, M.V., Clarke, D.J.B., Evangelista, J.E., Jenkins, S.L., Lachmann, A., Wojciechowicz, M.L., Kropiwnicki, E., Jagodnik, K.M., et al. (2021). Gene Set Knowledge Discovery with Enrichr. Curr. Protoc. 1, e90. https://doi.org/10.1002/cpz1.90.





STAR*METHODS

KEY RESOURCES TABLE

REAGENT or RESOURCE	SOURCE	IDENTIFIER
Antibodies		
Mouse monoclonal anti LAMIN A/C	Cell Signaling Technology	Cat# 4777; RRID: AB_10545756, clone 4C11, lot 5
Rabbit monoclonal anti GAPDH	Cell Signaling Technology	Cat# 2118; RRID: AB_561053, clone 14C10, lot 14
Rabbit polyclonal anti PGC-1-α	Novus	Cat# NBP1-04676; RRID: AB_1522118, clone Q9UBK2
Rabbit monoclonal anti PGC-1-β	Abcam	Cat# ab176328; RRID: AB_2893194, clone EPR12370
Rabbit monoclonal anti HSL	Cell Signaling Technology	Cat# 18381; RRID: AB_2798800, clone D6W5S, lot 1
Rabbit polyclonal anti HSL	Cell Signaling Technology	Cat# 4107; RRID: AB_2296900, lot 4
Mouse monoclonal anti HSL	Santa Cruz Biotechnology	Cat# sc-74489; RRID: AB_2135504, clone G-7, lot J0520
Rabbit polyclonal anti phospho-serine 660-HSL	Cell Signaling Technology	Cat# 4126; RRID: AB_490997, lot 3
Rabbit polyclonal anti phospho-serine 660-HSL	Cell Signaling Technology	Cat# 45804; RRID: AB_2893315, lot 1
Mouse monoclonal anti SFPQ	Abcam	Cat# ab11825; RRID: AB_298607, clone B92, lot GR33268352-14
Rabbit polyclonal anti SFPQ	Abcam	Cat# ab38148; RRID: AB_945424, lot GR3267048-3
Rabbit anti-nmt55/p54nrb (NONO)	Abcam	Cat# ab70335; RRID: AB_1269576, lot GR201728-56
Rabbit polyclonal anti UCP1	Abcam	Cat# ab10983; RRID: AB_2241462, lot GR3329095-1
Mouse monoclonal anti OXPHOS	Abcam	Cat# ab110411; RRID: AB_2756818, lot GR3272307-3
Rabbit monoclonal anti SMAD3	Abcam	ab40854; RRID: AB_777979, clone EP568Y, lot GR3255567-2
Rabbit monoclonal anti phospho serine423 and serine425 SMAD3	Abcam	Cat# ab52903; RRID: AB_882596, clone EP823Y, lot GR3248717-6
Mouse monoclonal anti SMAD4	Santa Cruz Biotechnology	Cat# sc-7966; RRID: AB_627905, clone B-8, lot L0220
Rabbit polyclonal anti ACC	Cell Signaling Technology	Cat# 3662; RRID: AB_2219400, lot 8
Rabbit monoclonal anti H3K9me2	Abcam	Cat# ab32521; RRID: AB_732927, clone Y79, lot GR3228498-2
Rabbit polyclonal anti RNApollI CTD	Abcam	Cat# ab26721; RRID: AB_777726, lot GR3305785-2
Rabbit polyclonal anti FABP4	Cell Signaling Technology	Cat# 2120; RRID: AB_2102466, lot 3
Rabbit polyclonal anti PKAc-alpha	Cell Signaling Technology	Cat# 4782; RRID: AB_2170170, lot 3
Rabbit monoclonal anti H3	Cell Signaling Technology	Cat# 4499; RRID: AB_10544537, clone D1H2, lot 9
Anti-rabbit horse radish peroxidase- labelled secondary antibody	Cell Signaling Technology	Cat# 7074; RRID: AB_2099233, lot 29, 30, 31, 32
Anti-mouse horse radish peroxidase- labelled secondary antibody	Cell Signaling Technology	Cat# 7076; RRID: AB_330924, lot 34, 35
Anti-mouse Alexa-fluor 488-conjugated	Invitrogen	Cat# A11029; RRID: AB_2534088
		(Continued on next na

Article



Continued				
REAGENT or RESOURCE	SOURCE	IDENTIFIER		
Normal Rabbit IgG	Cell Signaling Technology	Cat# 2729; RRID: AB_1031062		
Normal Mouse IgG	Santa Cruz Biotechnology	Cat# sc-2025; RRID: AB_737182, lot G2020		
Chemicals, peptides, and recombinant proteins				
CL-316,243	Sigma-Aldrich	Cat# C5976		
BAY 59-9435	NoValix	N/A		
Rosiglitazone	Cayman	Cat# CAY-7140-100		
Tris	Sigma-Aldrich	Cat# T1378		
nsulin (10 mg/mL)	Sigma-Aldrich	Cat# L9278		
Triiodothyronine	Sigma-Aldrich	Cat# T6397		
Transferrin	Sigma-Aldrich	Cat# T 8158		
IBMX	Sigma-Aldrich	Cat# I5879		
Dexamethasone	Sigma-Aldrich	Cat# D4902		
SB431542	Sigma-Aldrich	Cat# 616461		
TGFβ1	Peprotech	Cat# 100-21C		
Forskolin	Sigma-Aldrich	Cat# F6886		
Leptomycin B	Sigma-Aldrich	Cat# L2913		
DMSO	Sigma-Aldrich	Cat# D2650		
D-PBS	Sigma-Aldrich	Cat# D8537		
Cholesteryl[1- ¹⁴ C]oleate	PerkinElmer	Cat# NEC638		
Cholesteryl oleate	Sigma-Aldrich	Cat# C9253		
[1- ¹⁴ C] oleic acid	PerkinElmer	Cat# NEC317		
Oleic acid	Sigma-Aldrich	Cat# 01383		
Benzethonium hydroxide	Sigma-Aldrich	Cat# B2156		
L-carnitine	Sigma-Aldrich	Cat# C0158		
Sucrose	Sigma-Aldrich	Cat# S0389		
Dithioerythritol	Sigma-Aldrich	Cat# D9779		
Leupeptin	Sigma-Aldrich	Cat# L2884		
Antipain	Sigma-Aldrich	Cat# A6191		
Human fibroblast growth factor 2 (hFGF2)	Gibco	Cat# PHG0261		
L- Glutamine	ThermoFischer Scientific	Cat# 25030-024		
Collagenase Type I	Sigma-Aldrich	Cat# C0130		
Collagenase Type II	Worthington	Cat# LS004176		
Trypsin-EDTA	ThermoFischer Scientific	Cat# 25300-054		
Penicillin G 10 000U/mL & Streptomycin 10 000µg/mL	ThermoFischer Scientific	Cat# 2500-054 Cat# 15140-122		
Human FGF2 100 μg	PreproTech	Cat# 100-18B		
Hepes (1M)	Ozyme	Cat# BE 17-737E		
HAM's F12 with L-Glutamine	Ozyme	Cat# 12-615F		
DMEM low glucose (1g/L) with GlutaMAX	Gibco	Cat# 21885		
DMEM low glucose (1g/L)	Sigma-Aldrich	Cat# D6446		
DMEM high glucose (4.5 g/L) with	Sigma-Aldrich	Cat# D6429		
L-glutamine F12 Nutrient mixture	Gibco	Cat# 21765		
Trypsin-EDTA	Gibco	Cat# 25300		
Fetal bovine serum	Gibco	Cat# 10270, lot 42Q5881K		
Multiscribe Reverse Transcriptase	ThermoFischer Scientific	Cat# 4368813		
Fast SYBR Green Master Mix	ThermoFischer Scientific	Cat# 4485614		
Taqman Fast Advanced Master Mix	ThermoFischer Scientific	Cat# 4444558		
A magnetic bead	Invitrogen	Cat# 10002		
G magnetic bead	Invitrogen	Cat# 10003 (Continued on pext page)		

(Continued on next page)



Continued		
REAGENT or RESOURCE	SOURCE	IDENTIFIER
SDS-PAGE gel (420% gradient)	Biorad	Cat# 5678094 ou 5678095
Trans-Blot turbo RTA transfert kit, nitrocellulose membrane	Biorad	Cat# 1704271
Clarity Western ECL Substrate	Biorad	Cat# 170-5060
Clarity max Western ECL Substrate	Biorad	Cat# 1705062
O-(+) glucose	Sigma	Cat# G8270
Bovine serum albumin (BSA)	Sigma	Cat# A7030
Formalin solution	Sigma	Cat# HT501128
Paraformaldehyde	Sigma	Cat# 10267934
riton X-100	Sigma	Cat# T9284
Hoechst 33342	Invitrogen	Cat# H3570
n Situ Mounting Medium with DAPI	Sigma-Aldrich	Cat# DUO82040
Eosin G o Y 0.5% alcoholic	Diapath	Cat# C0353
Mayer hematoxylin	Diapath	Cat# C0303
Cacodylate buffer	EMS	Cat# 11655
EMbed812 resin	EMS	Cat# 14120
Histoclear II	National Diagnostics	Cat# HS-202
Sequencing Grade Modified Trypsin	Promega	Cat# V5111
S-Trap micro (≤100μg), 80 Pack	Protifi	Cat# C02-micro-80
ris(2-carboxyethyl)phophine	Sigma-Aldrich	Cat# C4706-10g lot 0000392536
2-Chloroacetamide	Sigma-Aldrich	Cat# C0267-100G
Acetonitrile gradient grade ≥ 99.9%	Sigma-Aldrich	Cat# 10000292500
Methanol gradient grade \geq 99.9%	Sigma-Aldrich	Cat# 1060072500
Formic Acid 98%-100%	Sigma-Aldrich	Cat# 5330020050
Frifluoroacetic acid > 99.0%	Sigma-Aldrich	Cat# 80457-10ML
richloroacetic acid	Sigma-Aldrich	Cat# T9159-250G
N-Lauroylsarcosine sodium salt	Sigma-Aldrich	Cat# 61743-25G
DL-Dithiothreitol	Sigma-Aldrich	Cat# D0632-5G
odoacetamide	Sigma-Aldrich	Cat# I6125-5G
riethanolamine	Sigma-Aldrich	Cat# 90279-100ML
Acrylamide/Bis-acrylamide solution	Sigma-Aldrich	Cat# A3699-5x100mL
,2-Bis(dimethylamino)ethane (TEMED)	Sigma-Aldrich	Cat# T9281-25ML
Stacking Gel Buffer for PAGE	Biorad	Cat# 1610799
Resolving Gel Buffer for PAGE	Biorad	Cat# 1610798
Ammonium Persulfate (APS)	Biorad	Cat# 1610700
Critical commercial assays		
NEFA C kit	Fujifilm Wako	Cat# SBDW1W434-91795; SBDW1W436-91995
Free Glycerol reagent	Sigma-Aldrich	Cat# F6428
Glucose GOD FS kit	DiaSys	Cat# 1 2500 99 10 026, lot 24781
nsulin ultrasensitive ELISA kit	ALPCO Diagnostics	Cat# 80-INSMS-E1
riglyceride reagent	Sigma-Aldrich	Cat# T2449
Lipofectamine 2000	Invitrogen	Cat# 11668-019
ipofectamine RNAimax	Invitrogen	Cat# 13778150
Neon transfection system kit	Invitrogen	Cat# MPK10096
Protein Subcellular Fractionation Kit for	Thermo Fisher Scientific	Cat# 87790
Nuclear Extract Kit	Active Motif	Cat# 40010
Nuclei EZ Prep	Sigma	Cat# NUC101-1KT
ONeasy kit	Qiagen	Cat# 69504
	a.ag	

(Continued on next page)

Article



Continued		
REAGENT or RESOURCE	SOURCE	IDENTIFIER
Qiazol buffer	Qiagen	Cat# 79306
RNeasy kit	Qiagen	Cat# 74106
DNasel	Invitrogen	Cat# 18068-015
BCA Protein Assay kit	ThermoFisher	Cat# 23225
Duolink In Situ Reagents	Sigma-Aldrich	Cat# DUO92101
DC Protein Assay Kit II	Biorad	Cat# 5000112
Seahorse XF Cell Mito Stress Kit	Agilent	103015
SurePrint G3 Human GE v3 microarray (8X60K)	Agilent	Design 072363
Experimental models: Organisms/strains		
Mouse: B6.129P2 <i>-Lipe</i> ^{tm1Rze} backcrossed > 10 times on C57BL/6J genetic background: C57BL6/J HSL KO mice	Rudolf Zechner, University of Graz	N/A
Mouse: Rj:SWISS <i>-Lipe</i> ^{em1Land} SWISS HSL-KO mice	This paper (Dominique Langin, I2MC)	N/A
Mouse: Rj:SWISS <i>-Lipe^{em2Land}</i> SWISS HSL-NLS mice	This paper (Dominique Langin, I2MC)	N/A
Oligonucleotides		
siRNA sequences are listed in Table S1		N/A
Oligonucleotide sequences used in quantitative PCR are listed in Table S2		N/A
Sequences of guide RNAs and single- stranded DNAs are listed in Table S3		N/A
Oligonucleotide sequences used in reverse transcription-quantitative PCR are listed in Table S4		N/A
Software and algorithms		
GraphPad Prism (version 9.5.0 for PC, version 10.01 for Mac)	GraphPad	https://www.graphpad.com
QuPath-0.3.0	QuPath-0.3.0.lnk	N/A
Maxquant	Max Planck Institute of Biochemistry	https://www.maxquant.org/
Perseus	Max Planck Institute of Biochemistry	https://maxquant.net/perseus/
Spectronaut	Biognosys	N/A
Other		
Glucometer	Roche SAS	Glucotrend Accu-Chek Performa
Mouse: Chow diet	Ssniff	V1534
Mouse: 60% high-fat diet	Ssniff	E15742-347
Microporator	Invitrogen	Neon Electroporation system
SeaHorse XFe24 Analyzer	Agilent	N/A
Confocal LSM780 and LSM900	Zeiss	N/A
	Hamamatsu	nanozoomer
Slide scanner system UltiMate 3000 RSLCnano system	Thermo Fisher Scientific	N/A
•	Thermo Fisher Scientific Thermo Fisher Scientific	
Q Exactive Plus Hybrid Quadrupole- Orbitrap Mass Spectrometer		N/A
TIMS-TOF SCP mass spectrometer	Bruker	N/A
HT 7700 Transmission electron microscope	Hitachi	N/A
Quant Studio 5	ThermoFisher	N/A
Deposited data		
Data S1 – Uncropped Scans and Source Data	This paper	N/A





EXPERIMENTAL MODEL AND STUDY PARTICIPANT DETAILS

Mouse models

Mice were housed at 22°C on a 12-h light (7am-7pm), 12-h dark cycle and manipulated according to Inserm guidelines and European Directive 2010/63/UE in the local animal care facility (agreements A 31 555 008, B 31 555 011 and C 31 555 011). Protocols were approved by the French Ministry of Research (APAFIS #34176-2021112915333477) after review by local ethics committee (comité d'éthique en expérimentation animale de l'UMS006/CREFRE, CEEA122, Toulouse, France).

HSL-KO mice on the C57BL6/J genetic strain have been previously described. ⁵⁶ We used one cell embryos from Swiss-CD1 mice to produce novel knock-in and knock-out mouse models. Five- to seven-week-old female mice were superovulated as previously described. ⁵⁷ Zygotes were kept in KSOM medium (Merck-Sigma) in a water jacketed CO₂ incubator (5% CO₂, 37°C) until electroporation.

In silico analysis was performed using CRISPOR freeware (http://crispor.tefor.net).⁵⁸ To produce HSL-KO Swiss mice, guide RNA (sgRNA) were designed in exon 6 (Table S3). To produce knock-in Swiss mice expressing HSL-NLS, sgRNA and single-strand DNA (ssDNA) containing three copies of the SV40 T-antigen NLS and homology arms were designed to target the end of the coding region in Lipe exon 9 nearby the Stop codon. sgRNAs and ssDNA were chemically synthesized by IDT and stored at -80°C until use. Efficacies of sgRNAs were first tested in mouse embryonic fibroblasts. Following genomic DNA extraction, T7 endonuclease tests were performed on amplicons.

To induce modifications in the *Lipe* locus, SpyCas9-NLS was complexed with sgRNAs. Aliquots of sgRNA were denaturated at 80 °C for 2 min and then put on ice 2 min before adding the protein. The complex was performed at 1.3-1.7:1 (sgRNA:Cas9 protein) molar stoichiometry. Cas 9 protein and sgRNA were incubated 10 min at room temperature and kept on ice during electroporation. For knock-in experiments, ssDNA was added together with the Cas9 protein. Electroporation was performed as previously described.⁵⁷ Zygotes were then transferred into KSOM medium and kept in an incubator until reimplantation into the oviduct of Swiss-CD1 or B6CBA/F1 (Janvier Labs, France) pseudopregnant females (10–15 embryos per female).

Cell models

Human multipotent adipose-derived stem cells (hMADS3 herein referred to as hMADS) and hMADS2 cells, derived from two different donors, were used between passages 16 and 25.²² Cells were seeded at a density of 5000 cells/cm² in DMEM supplemented with 10% fetal bovine serum (Gibco), 15 mM Hepes, 2.5 ng/ml hFGF2, 60 mg/mL penicillin, and 50 mg/mL streptomycin. hFGF2 was removed when cells reached confluence. Cells were triggered for differentiation at day 2 post-confluence (designated as day 0) in DMEM/Ham's F12 media supplemented with 10 mg/mL transferrin, 10 nM insulin, 0.2 nM triiodothyronine, 1 mM dexamethasone, 500 mM IBMX and 100 nM rosiglitazone. After three days, the culture medium was replaced with one lacking dexamethasone and IBMX. On day 9, rosiglitazone was removed to promote differentiation toward white adipocytes. When indicated, adipocytes were directed towards a beige phenotype by addition of 100 nM of the PPARγ agonist, rosiglitazone, between day 14 and day 18.

Human primary preadipocytes were obtained from subcutaneous adipose tissue of 25 obese men included the MONA (NCT02161926) clinical trial conducted at the Clinical Investigation Center, Inserm, Toulouse University Hospital, France. ⁵⁹ The study was approved by Comité de Protection des Personnes and Agence Nationale de Sécurité du Médicament et des produits de santé (ANSM), France. Volunteers provided informed consent before participation in the studies. Subcutaneous abdominal adipose tissue was digested with collagenase type I (Sigma-Aldrich). Following filtration (250 μ M) and centrifugation (10 min at 300g), the pellet containing cells from the stromal vascular fraction was incubated for 10 min in erythrocyte lysis buffer. Cells were then filtrated (70 μ M), centrifuged (10 min at 300g), resuspended in PM4 proliferation medium with 132 nM insulin and plated into 35 mm Petri dish. ⁶⁰ PM4 was replaced every second day. Cells were sub-cultured at 70% confluence. Differentiation of 2-day post-confluent cells was induced by DMEM/HamF12 medium supplemented with 66 nM insulin, 1 μ M dexamethasone, 1 nM triiodothyronine, 0.1 μ g/mL transferrin, 0.25 mM IBMX, and 1 μ M rosiglitazone. After 6 days, rosiglitazone and IBMX were omitted and dexamethasone was replaced with 0.1 μ M cortisol. ^{59,61,62}

Total stromal vascular fraction from HSL-WT and HSL-KO mice was isolated from inguinal fat depot. 61 Briefly, tissue was minced and incubated for 45min in PBS supplemented with 1% BSA (Sigma-Aldrich) and collagenase type II (Worthington). Single cell suspension was then passed through a 45 μ m filter and spun at 300g for 5 min. The supernatant was discarded and the total SVF seeded in DMEM supplemented with 10% fetal bovine serum and Penicillin-Streptomycin. Once at confluence, adipogenic differentiation was induced by supplementing the media with rosiglitazone (1μ M), IBMX (125μ M), dexamethasone (100nM) and insulin (17nM) for 3 days, then only insulin for 4 additional days.

HEK293T cells (ATCC-CRL-3216) were cultured in DMEM supplemented with 10% fetal calf serum (Invitrogen).

METHOD DETAILS

Measurements in human cells

RNA interference

RNA interference was achieved by siRNA. Briefly, on day 7 of differentiation, hMADS cells were detached from culture dishes with trypsin-EDTA (Invitrogen). Control siRNA against green fluorescent protein and gene-specific siRNA for *LIPE* (Eurogentec), *PPARGC1A* (pool of 4 siRNAs, Dharmacon), *PNPLA2* (Eurogentech), *SMAD3* (Invitrogen) and *SMAD4* (Ambion) were delivered

Article



into adipocytes using a microporator (Neon Electroporation system, Invitrogen) (1100 V, 20 ms, 1 pulse). Sequences are shown in Table S1. For measurement of oxygen consumption in hMADS adipocytes and of gene expression in human primary adipocytes, siRNA was delivered using Lipofectamine RNAimax (Invitrogen) according to the manufacturer's protocol.

Pharmacological treatments

Chronic inhibition of HSL activity was achieved between day 7 and 18 of hMADS preadipocyte differentiation using 1μ M of BAY 59-9435 (NoValix), a selective HSL enzymatic inhibitor. ²⁵ Inhibition of type I TGF β receptor-mediated SMAD3 phosphorylation was achieved using 10 μ M SB431542 (Sigma) between day 14 and 18 of differentiation. TGF β 1 (Peprotech) was used at 5ng/mL for 3 h to assess SMAD3/HSL nuclear translocation, and 24 h to measure *PPARGC1A* mRNA levels. HSL phosphorylation was induced using 10 μ M of the adenylyl cyclase activator, forskolin (Sigma). The CRM1 exportin inhibitor, leptomycin B (Sigma), was used for 8 h at 50 nM to investigate HSL nuclear transport.

Oxygen consumption rate

hMADS preadipocytes were seeded and differentiated into 24 multi-well plates (Seahorse Bioscience). Oxygen consumption rate (OCR) was determined using an XF24 Extracellular Flux Analyzer (Seahorse Bioscience). Cells were incubated 1 h at 37°C in unbuffered XF assay medium supplemented with 2 mM GlutaMAX, 1 mM sodium pyruvate and 10 mM glucose. Mito stress test was achieved through subsequent additions of oligomycin (1.2 μ M), FCCP (1 μ M), and rotenone/antimycin A (2 μ M each). Basal OCR was calculated by subtraction of rotenone and antimycin A-induced OCR from the unstimulated OCR value. Maximal respiration was determined using FCCP. Proton leak was calculated by subtraction of FCCP-induced to rotenone and antimycin A-induced OCR.

Mitochondrial DNA quantitation

Cells were scrapped in PBS and total DNA was extracted using DNeasy kit (Qiagen). Primers used in real-time quantitative PCR are shown in Table S2. Mitochondrial DNA quantitation was calculated as $\Delta\Delta$ Ct of the mitochondrial genes *NAD1* or *NAD4* using *LPL* as a nuclear housekeeping gene.

Oleate oxidation assays

For oleate oxidation assays, cells in six-well plates were incubated during 3 h in 1 ml Krebs-Ringer buffer with 3% BSA, 1 mM L-carnitine, 80 μ M oleic acid, 1 μ Ci/ml [1-¹⁴C] oleic acid (PerkinElmer). Medium was then transferred and acidified with 1 M sulfuric acid in closed vials containing a central well filled with benzethonium hydroxide (Sigma). After 2 h incubation, trapped ¹⁴CO₂ was measured by liquid scintillation counting in Tri-Carb 2100TR (Packard). Cells were washed and then scraped in cold buffer PBS 0,1% SDS for protein normalization.⁶³

Chromatin isolation

For preparation of cytosolic and chromatin extracts for protein quantitation, hMADS adipocytes were fractionated using Protein Subcellular Fractionation Kit for Tissues (Thermo Fisher Scientific) according to the manufacturer's instruction.

DNA microarray

Total RNA from white and beige hMADS adipocytes transfected with HSL (siLIPE) and green fluorescent protein (as control, siCTR) targeting siRNAs was used to prepare Cyanine-3-labeled cRNA for hybridization on a SurePrint G3 Human GE v3 microarray (8X60K, Design 072363). Experimental protocol and data analyses were performed as described. ⁵⁷ Gene expression data have been deposited at the NCBI's public data repository Gene Expression Omnibus (https://www.ncbi.nlm.nih.gov/gds/) with the dataset identifier GSE186544.

DNA constructs and cell transfection

HEK293T cells were transfected using lipofectamine 2000 (Invitrogen) with $1\mu g$ each of pcDNA3 expressing native human HSL, short inactive HSL (HSL(s)), nuclear export signal-deleted HSL (HSL Δ NES) or nuclear localization signal-tagged HSL (HSL-NLS) as well as empty plasmids. HSL(s) and HSL Δ NES were respectively obtained from a naturally occurring isoform that skips exon 6^{24} and a deletion between residues 566 to 580. Three copies of the SV40 T-antigen NLS were inserted at the C-terminus of HSL to produce HSL-NLS. hMADS preadipocytes were transduced with adenoviral particles encoding HSL-NLS (VectorBiolabs).

In situ proximity ligation assay and immunofluorescence

Cells were fixed with 4% paraformaldehyde (Sigma) for 15 min and permeabilized for 10 min at room temperature with 0.2% Triton X-100 (Sigma). The following primary antibodies were incubated overnight at 4 °C: anti-HSL (murine antibody sc-74489, Santa Cruz Biotechnology or rabbit antibody, 18381, Cell Signaling Technology), anti-SMAD3 (rabbit antibody ab40854, Abcam), anti-SMAD4 (murine antibody sc-7966, Santa Cruz), anti-SFPQ (rabbit antibody ab38148, Abcam), anti-NONO (rabbit anti-nmt55/p54nrb ab70335, Abcam) and anti-RNAPollI (rabbit antibody ab26721, Abcam). *In situ* proximity ligation assays were performed using Duolink In Situ reagents (Sigma). Incubation of antibodies, ligation of oligodeoxynucleotides and amplification were performed according to the manufacturer's instructions. For immunofluorescence assays, the anti-mouse (Alexa-fluor 488-conjugated, A11029, Invitrogen, 1/300) secondary antibody was incubated for 45 min. Nuclei were labelled with Hoechst 33342 or DAPI. Confocal microscopy was performed using Zeiss LSM780 or LSM900. Image processing was similar for all conditions and the same settings were applied to images. To measure HSL density in human adipocyte cytosol and nucleus, images were obtained using a Zeiss LSM900 confocal microscope. 3D images were acquired with the Airyscan2 detector, SR acquisition mode and scaling per pixel 0.035 μm x 0.035 μm x 0.150 μm. Raw images were processed with the ZEN Airyscan interface. HSL fluorescence was measured in the nuclei and cytosol using the FIJI software and MorphoLibJ plugin. ^{64,65} First, an image plane at the center of the nuclei was selected on each image, then saved with an overlay including a drawing of the cell contour. Then ImageJ macro was used to open each image, segment the nuclei using Li auto-threshold on DAPI signal, segment the cytosol





by using the cell drawing and excluding lipid droplet with a Huang auto-threshold on HSL signal and measure HSL mean intensity on the resulting nucleus and cytosol segmentation. The macro is available on github [https://github.com/remyff/Nucleii-HSL/blob/main/nuclei_cell_AS_intensities_file_.ijm].

Analysis of HSL interactomes following immunoprecipitation

Protein samples from hMADS adipocytes were processed for trypsin digestion using an S-trap micro device (Protifi) according to the manufacturer's instructions, except that protein digestion using trypsin was performed overnight at 37 °C. Peptides were analyzed by nanoLC-MS/MS using an UltiMate 3000 RSLCnano system coupled to a Q-Exactive Plus mass spectrometer (Thermo Fisher Scientific, Bremen, Germany) using the same settings as for the secretome analysis (see below) except that peptides were eluted using a shorter gradient (5 to 50% gradient of solvent B over 60 min). Raw mass spectrometry files were processed with the MaxQuant software (version 2.1.4.0). Data were searched against human entries of the reference proteome database (Proteome ID UP000005640, last modified February 17, 2023) and the Perseus toolbox (version 2.0.10.0) was used for the imputation of missing values. Proteins with statistically varying abundance between targeted bait experiments in triplicates and IgG control experiments in triplicates were identified using a Student's t-test (p-value < 0.05). Additionally, a protein was considered enriched only when it had at least a 2-fold change over the IgG controls. The volcano plots were generated by plotting the -log10 of the p-value, calculated by a student's t-test comparing bait/IgG triplicates, against the fold change (which corresponds to the average fold change between bait/IgG triplicates).

Protein analyses in human adipocyte culture media

For each sample, 2 ml of conditioned medium were first cooled on ice. Sodium lauroyl sarcosinate was added to a final concentration of 0.1%. After mixing, TCA was added to a final 7.5% concentration, and the solution was precipitated on ice for 2h. The mixed protein-detergent precipitate was collected by centrifugation ($10,000 \times g$, 10 min at 4°C). The supernatant was carefully removed and the pellet was washed four times with 2 ml of tetrahydrofuran (precooled in ice). Finally, the pellet was redissolved in 100 μ l of 40 mM Tris pH 6.8, 2% SDS, 10% glycerol with the help of a sonicator bath for 15 min. The protein concentration was determined using the DCTM Protein Assay kit (Bio-Rad). 30 μ g of proteins were reduced with 25mM DTT for 5 min at 95 °C and alkylated with 90mM iodoacetamide for 30 min at room temperature in the dark. Protein samples were loaded onto a 1D SDS-PAGE gel (0.15 x 8 cm) and the electrophoretic migration was stopped as soon as the proteins entered the separating gel, in order to isolate all proteins in a single gel band. The corresponding gel slice was excised and washed with 100 mM ammonium bicarbonate buffer. Proteins were in-gel digested using 1μ g of modified sequencing grade trypsin (Promega) in 50 mM ammonium bicarbonate overnight at 37 °C. The resulting peptides were extracted in 50 mM ammonium bicarbonate followed by 10% formic acid/acetonitrile (1/1 v/v). The peptidic fractions were dried under speed-vacuum and resuspended with 5% acetonitrile, 0.05% trifluoroacetic acid for further MS analysis.

Peptides were analyzed by nanoLC-MS/MS using an UltiMate 3000 RSLCnano system coupled to a Q-Exactive Plus mass spectrometer (Thermo Fisher Scientific, Bremen, Germany) as previously described, 66 except that peptides were eluted using a 5 to 50% gradient of solvent B over 300 min at a flow rate of 300 nL/min. Raw mass spectrometry files were processed with the MaxQuant software (version 1.5.2.8) for database search with the Andromeda search engine and quantitative analysis. Data were searched against human entries of the reference proteome database (Proteome ID UP000005640, last modified March 7, 2021). Carbamidomethylation of cysteines was set as a fixed modification, whereas oxidation of methionine and protein N-terminal acetylation were set as variable modifications. Specificity of trypsin digestion was set for cleavage after K or R and two missed trypsin cleavage sites were allowed. The precursor mass tolerance was set to 20 ppm for the first search and 4.5 ppm for the main Andromeda database search. Minimum peptide length was set to seven amino acids and the minimum number of unique or razor peptides was set to one for validation. Andromeda results were validated by the target decoy approach using a reverse database, with a false discovery rate set at 1% for both peptide sequence match and protein level. For label-free relative quantification of the samples, the match between runs option of MaxQuant was enabled with a match time window of 0.7 min to allow cross-assignment of MS features detected in the different runs after alignment of the runs with a time window of 20 min. Protein quantification was based on unique and razor peptides and the minimum ratio count was set to 1 for label-free quantification. The "LFQ" metric from the MaxQuant "protein group.txt" output was used to quantify proteins. The LFQ values were log2 transformed using the Perseus toolbox (version 1.6.7.0) and missing values were replaced by random numbers drawn from a normal distribution with a width of 0.3 and down shift of 1.8. For statistical analysis, a two-tailed Welch t-test allowing for unequal variance between groups was performed, followed by the Benjamini-Hochberg false-discovery rate correction for multiple testing. Graphs are plotted as raw p-values and reported as significant only if the adjusted p < 0.05.

Protein analyses in human adipocyte nuclear extracts

Proteins were digested on S-trap devices (Protifi) and 50 ng of the resulting peptides were analyzed by nanoLC-MS/MS using an UltiMate 3000 RS nanoLC system (ThermoFisher Scientific) coupled to a TIMS-TOF SCP mass spectrometer (Bruker). Peptides were separated on a C18 Aurora column (25 cm x 75 μ m ID, IonOpticks) using a gradient ramping from 2% to 20% of B in 30 min, then to 37% of B in 3 min and to 85% of B in 2 min (solvent A: 0.1% formic acid in H₂O; solvent B: 0.1% formic acid in acetonitrile), with a flow rate of 150 nL/min. MS acquisition was performed in DIA-PASEF mode on the precursor mass range [400-1000] m/z and ion mobility 1/K0 [0.64-1.37]. The acquisition scheme was composed of 8 consecutive TIMS ramps using an accumulation time of 100 ms, with 3 MS/MS acquisition windows of 25 Th for each of them. The resulting cycle time was 0.96s. The collision energy was ramped linearly as a function of the ion mobility from 59 eV at 1/K0=1.6Vs cm-2 to 20 eV at 1/K0=0.6Vs cm-2.

All raw files were processed using Spectronaut (version 19) with a library free approach (directDIA+) using the human reference database from the Uniprot 2024 release. Protein validation and quantification were performed using default BGS factory settings.

Article



Briefly, carbamidomethylation of cysteines was set as a fixed modification, whereas oxidation of methionine and protein N-terminal acetylation were set as variable modifications. Specificity of trypsin digestion was set for cleavage after K or R and two missed trypsin cleavage sites were allowed. Quantification was performed on MS2 level and the iBAQ metric was used to provide a measure of protein absolute abundance. ¹³ Proteins were ranked according to the mean value of iBAQ intensity in the three biological replicates. The mass spectrometry proteomics data have been deposited to the ProteomeXchange Consortium via the PRIDE partner repository (https://www.ebi.ac.uk/pride/) with the dataset identifiers PXD043860 (interactome), PXD029261 (secretome) and PXD060011 (nuclear proteome).

Measurements in mouse models

Nutritional challenges

In fasting-refeeding experiments, Swiss-CD1 male mice (Janvier Labs, France) were fasted at ZT0 and killed at ZT16 or re-fed at ZT12 and killed at ZT16. For high-fat diet challenge, mice were fed a diet containing 60% fat (Ssniff E15742).

Adipose tissue histology

Freshly collected tissue was fixed in 4% formalin (Sigma) for 24h at room temperature and dehydrated using ethanol and histoclear II (Electron microscopy Sciences). Following paraffin embedding, blocks were cut in 4 µm slices. Following hematoxylin-eosin staining, images were obtained with Hamamatsu nanozoomer and visualized using NDP view (Hamamatsu photonics).

Mating trials

Five to six male mice from each group were individually housed with two sexually mature virgin Swiss-CD1 females. Vaginal plugs were checked daily and the development of gestation was monitored for one month. The size of the litter was recorded.

Adeno-associated viral vectors

The expression cassette was obtained by cloning, between the inverted terminal repeats, an optimized mouse HSL, with Ser423Ala mutation, coding sequence under the control of CMV promoter. A non-coding cassette carrying the CMV promoter, but no transgene, was used to produce null vectors. Single-stranded adeno-associated viral vectors of serotype 8 were produced by triple transfection in HEK293 cells and purified using an optimized CsCl gradient-based purification protocol that renders vector preparations of high purity and devoid of empty capsids. Two groups of C57BL6/J HSL-KO/HSL-WT heterozygous male mice fed chow diet⁶⁷ were injected with adeno-associated viral (AAV) vectors expressing no protein (null vector) or HSL-S423A-NLS (5x10¹¹ vg per fat pad). Prior to injection, the two groups showed similar glucose tolerance. Glucose tolerance test and collection of adipose tissue and blood samples were performed 5 and 6 weeks post-injection, respectively.

HSL enzymatic activity

Cholesteryl ester hydrolase activity was measured in perigonadal adipose tissue. 69 Total protein was extracted with homogenization buffer (0.25 M sucrose, 1 mM EDTA, pH 7.0, 1 mM dithioerythritol, 20 ug/ml leupeptin, 20 ug/ml antipain). Briefly, 14 C-labelled and unlabelled cholesteryl oleate were emulsified with phospholipids by sonication. Fat-depleted BSA (Sigma-Aldrich) was used as fatty acid acceptor. Protein cytosolic fractions were incubated for 30 min at 37 $^{\circ}$ C with the substrate. Hydrolysis was stopped, and radiolabelled fatty acids were extracted and counted using a scintillation counter (Tri-Carb 2100TR, Packard). Enzyme specificity was checked using 1μ M of the HSL inhibitor, BAY 59-9435.

Mouse adipose tissue explants

Mouse subcutaneous adipose tissue was minced into pieces of around 1-2 mm and rinsed with PBS.⁶¹ Explants were then incubated in Krebs-Ringer Buffer with 2% BSA and 2 mM glucose at 37°C. 10ng/mL of TGFβ1 was added during 4h before harvest and snap freezing. Subcellular fractionation was performed as described for freshly isolated adipose tissue.

Isolation of mouse adipocyte nuclei

One hour following CL316,243 (1mg/kg) or vehicle intraperitoneal injection, adipocyte nuclei were isolated using a modified nuclear isolation protocol.⁴¹

Glucose tolerance test

Around 2 pm, 2 mg/g body weight of D-(+) glucose (Sigma) was administered by intraperitoneal route to 6h fasted mice. ⁶⁹ Glycemia was checked on blood from tail vein 30min before glucose injection and then at various times after glucose administration with a glucometer (Glucotrend Accu-Chek Performa, Roche SAS).

Blood analyses

Plasma glycerol was measured by enzymatic assay (Free Glycerol reagent, Sigma), non-esterified fatty acid and triacylglycerol levels were measured using the NEFA C kit (Fujifilm) and triglyceride reagent (Sigma), respectively. Glucose levels were measured using a glucometer or Glucose GOD FS kit (DiaSys). Plasma insulin was measured using an ultrasensitive ELISA kit (ALPCO Diagnostics).

Electron microscopy

Differentiated mouse preadipocytes from HSL-WT and HSL-KO mice were fixed with 2% glutaraldehyde in 0.1 M Sorensen phosphate buffer (pH = 7.4) for 1 h, washed with 0.1 M Sorensen phosphate buffer for 12 h and postfixed with OsO₄ in Sorensen phosphate buffer (Sorensen phosphate 0.05 M, glucose 0.25 M, OsO4 1%) for 1 h. Samples were dehydrated in an ascending ethanol series and embedded in epoxy resin (Epon 812, Electron Microscopy Sciences). After 24 h of polymerisation at 60 °C, ultrathin sections (70 nm of thickness) were mounted on 150 mesh collodion-coated nickel grids. For immunostaining, sections were incubated at 4°C with cold acetone for 30 min, blocked with 0.1%BSA-5%NGS-0.2%Tween 20 in PBS 1X (pH 7.4) for 15 min at room temperature. Sections were than incubated for 12 h at 4 °C with rabbit anti HSL antibody (Cell Signaling Technology), washed in 0.1% BSA-PBS before incubation for 1 h at room temperature with ultrasmall gold-conjugated goat anti rabbit. After silver enhancement reaction





(Aurion R-Gent SE-EM) and washing in PBS 1X, samples were fixed for 5 min in 1% glutaraldehyde and washed with distilled water. After poststained with 2% uranyl acetate in 50% ethanol grids were examined on a HT 7700 Hitachi electron microscope at an accelerating voltage of 75 kV.

Measurements common to mouse and human models

Gene and protein expression analysis

Reverse transcription-real-time quantitative PCR and Western Blot analyses were performed as described.

PCR primers and assay-on-demands

PCR primers and assay-on-demands

PCR primers and assay-on-demands

See Table S4.

Antibodies for western blotting

Antibodies were used at 1/1000 dilution. LAMIN A/C (4777, Cell Signaling Technology), GAPDH (2118, Cell Signaling Technology), PGC-1 α (NBP1-04676, Novus), PGC-1 β (ab176328, Abcam), HSL (18381 and 4107, Cell Signaling Technology), HSL-P660 corresponding to Ser⁶⁵⁰ in human HSL (4126 and 45804, Cell Signaling Technology), SFPQ (ab11825 and ab38148, Abcam), NONO (ab70335, Abcam), UCP1 (ab10983, Abcam), OXPHOX (ab110411, Abcam), SMAD3 (ab40854, Abcam), P-SMAD3 (ab52903, Abcam), SMAD4 (sc-7966, Santa Cruz), ACC (3662, Cell Signaling Technology), H3K9me2 (ab32521, Abcam), RNApolII (ab26721, Abcam), FABP4 (2120, Cell Signaling Technology), catalytic subunit of PKA (4782, Cell Signaling Technology) and H3 (4499, Cell Signaling Technology). Anti-rabbit IgG, anti-mouse IgG or protein A coupled to horseradish peroxidase were used as secondary antibodies.

Subcellular fractionation

Protein nuclear and cytosolic fractions from hMADS adipocytes and mouse adipose tissues were prepared using Nuclear Extract Kit (40010, Active Motif). Cells were rinsed with PBS and immediately scraped into 1x hypotonic buffer. Adipose tissue pads were ground in liquid nitrogen and lyzed by dounce into 1x hypotonic buffer. Subsequent steps followed the manufacturers' protocols. Antibodies to cytosolic and nuclear markers were used as indicated to analyze the purity of cellular fractions. To correct for variations in total HSL expression influencing nuclear pool quantitation, HSL nuclear accumulation was calculated as follows: [nuclear level/(cytosolic level + nuclear level)]. For nuclear RNA isolation, hMADS adipocytes were prepared using Nuclei EZ Prep (NUC101-1KT, Sigma) according to the manufacturer's instruction. Nuclear extracts were resuspended in RLT-β mercaptoethanol 1% (Qiagen). Gene expression was assessed as described above.

Immunoprecipitation

For endogenous nuclear co-immunoprecipitation in hMADS adipocytes, nuclear extracts were resuspended in lysis buffer (50 mM Tris pH8, 150 mM NaCl, 5 mM EDTA, 0.5% NP40). Preclearing was performed incubating nuclear extracts with 40 μ L protein A or G magnetic beads (Invitrogen) at 4 °C for 1h. Beads were discarded and supernatants were incubated with 5 μ g anti-HSL (4107, Cell Signaling Technology) or 8 μ g anti-SMAD3 (ab40854, Abcam), 7 μ g anti-SMAD4 (sc-7966, Santa Cruz), 7 μ g anti-SFPQ (ab11825, Abcam) and 7 μ g NONO (ab70335, Abcam) overnight at 4 °C. As a negative control of immunoprecipitation, respective amounts of control rabbit (2729, Cell Signaling Technology), or mouse (sc-2025, Santa Cruz) IgG was used. 25 μ L protein A or G magnetic beads were added for 20min at 4 °C. Beads were washed four times with lysis buffer before elution in 2x Laemmli buffer. For endogenous co-immunoprecipitation in mouse adipose tissue, frozen fat was crushed into powder using a mortar. For whole extract, tissue powder was lyzed into lysis buffer for 1 h at 4°C. Nuclear extracts were resuspended in lysis buffer up to 500 μ L. Further steps are identical to the ones described above for hMADS adipocytes.

QUANTIFICATION AND STATISTICAL ANALYSIS

All data are mean ± s.e.m. In cell culture experiments, the number of wells and cell passages are indicated in the Figure legends. In other experiments, the number of biologically independent experiments are shown. In mouse experiments, animals were assigned to groups randomly. Experiments were not blinded. Sample sizes were determined on prior literature and previous data from the laboratory in the respective mouse strains. Statistical analyses and graphical representations were performed using GraphPad Prism 9. Outliers were detected using the Grubbs' test. Following D'Agostino-Pearson and Shapiro-Wilk normality tests, parametric (unpaired Student's t-test, one-way ANOVA) or non-parametric (Mann-Withney, Kruskal Wallis) tests were used as indicated. Two-Way ANOVA with Sidak post-hoc test and Spearman correlation test were used as indicated. All tests were two-tailed. Confidence level was 95%. Statistical tests for large data sets are described in relevant sections (DNA microarray and proteomic analyses). Pathway analysis was performed using the ENRICHR web-based tool. 70,71